CORNICHON HOMOLOG 5-dependent ER export of membrane cargoes in phosphate-starved *Arabidopsis* root as revealed by membrane proteomic analysis

Tzu-Yin Liu,[1,2,†,*] Ming-Hsuan Tsai,[1,†] Jhih-Yi Wang,[1,†] Hui-Fang Lung,[1] Chiao-An Lu,[1] Chang-Yi Chiu,[1] Hong-Xuan Chow[1]

[1]Institute of Bioinformatics and Structural Biology, College of Life Sciences and Medicine, National Tsing Hua University, Hsinchu 30013, Taiwan.

[2]Department of Life Science, College of Life Sciences and Medicine, National Tsing Hua University, Hsinchu 30013, Taiwan.

[†]These authors have contributed equally to this work.

[*]Corresponding author:

Tzu-Yin Liu

Email: tzliu@life.nthu.edu.tw

Short title: Membrane proteomics of Pi-starved *cnih5* root

Keywords: CORNICHON HOMOLOG, ER cargo receptor, coat protein complex II (COPII), phosphate starvation, phosphate transporter, 4-hexylphenylazosulfonate (Azo), membrane proteomics

Abstract

Developing plants tolerant of low phosphate (Pi) availability is essential to reduce reliance on fertilizers and achieve agricultural sustainability. One strategy is to enhance the endoplasmic reticulum (ER) export of cargoes associated with Pi starvation and their trafficking to final destinations. However, the mechanisms underlying this process are underexplored. We recently discovered that *Arabidopsis thaliana CORNICHON HOMOLOG 5* (*AtCNIH5*) encodes a Pi deficiency-induced ER cargo receptor that regulates Pi homeostasis. To find potential membrane cargoes of *At*CNIH5, we applied the UV-cleavable 4-hexylphenylazosulfonate (Azo)-solubilized microsomal protein extraction for iTRAQ-based proteomic analysis. We identified 4,317 proteins in Pi-limited *Arabidopsis* roots, with 372 upregulated and 106 downregulated proteins in *cnih5*. Besides PHOSPHATE TRANSPORTER 1 proteins (PHT1s), downregulation of the biosynthetic or modifying enzymes for cell wall polysaccharides, very long-chain fatty acids, and their derivative extracellular aliphatic compounds is over-represented. Using the yeast split-ubiquitin and the *in-planta* tripartite split-GFP assays, we verified the interaction of *At*CNIH5 with various downregulated transporters in *cnih5*, including *At*PHT1s, *At*OCT1, *At*URGT6, *At*DTX21, and *At*DTX35. In addition, we demonstrated that the C-terminal acidic residue of *At*CNIH5 is required for interaction with *At*OCT1 but not with *At*PHT1;1 or *At*DTX21, indicating distinct cargo selection mechanisms. More importantly, enhancing *in-situ At*CNIH5 expression/activity enhances plant growth. By analogy with transcriptional factors that govern gene expression, we propose that *At*CNIH5 acts as a low Pi-responsive hub to facilitate ER export of specific membrane cargoes, providing a potential engineering strategy to improve plant fitness under suboptimal Pi supply.

Introduction

Phosphorus (P) is an essential macronutrient for plant growth and development (Poirier and Bucher, 2002; Poirier et al., 2022). Due to the low concentration of inorganic phosphate (Pi) in soil, the primary form of P that plants absorb, applying Pi fertilizer has become a common practice to improve crop productivity. However, the limited mobility of Pi in soil prevents plants from acquiring most applied Pi fertilizer, leading to P runoff into aquatic ecosystems. Therefore, developing plants with increased Pi uptake and high-use efficiency is crucial for minimizing Pi fertilizer usage, thereby reducing environmental pollution and promoting agricultural sustainability.

To adapt to low Pi bioavailability, plants employ various strategies to enhance external Pi acquisition and internal Pi remobilization, involving distinct Pi transporters in distinct subcellular compartments. *PHOSPHATE TRANSPORTER 1* (*PHT1*) genes encode the plasma membrane (PM)-localized Pi transporters responsible for the uptake and the intercellular translocation of Pi. Even though Pi deprivation upregulates most *PHT1* genes at the transcript level, the translation, secretion, and recycling rate of PHT1 proteins (PHT1s) also determine their abundance at the PM (Nussaume et al., 2011). Multiple post-translational mechanisms have been elucidated to regulate the protein level and the PM localization of PHT1s. The plant-specific SEC12-related PHOSPHATE TRANSPORTER TRAFFIC FACILITATOR1 (PHF1) contributes to the accumulation of PHT1s at the PM by assisting the PHT1s transit through the endoplasmic reticulum (ER) (González *et al.*, 2005; Bayle *et al.*, 2011; Chen *et al.*, 2015). The rice casein kinase II (CK2) diminishes the interaction between *Os*PT8 and *Os*PHF1 by phosphorylating *Os*PT8, thereby leading to ER retention of *Os*PTs (Chen et al., 2015). On the contrary, the protein phosphatase type 2C *Os*PP95 acts antagonistically with *Os*CK2 (Yang et al., 2020). In addition, under Pi sufficiency, the ubiquitin-conjugating E2 enzyme UBC24/PHOSPHATE2 (PHO2) at the ER or post-ER compartments mediates the ubiquitination of the endomembrane-associated *At*PHT1s followed by the vacuolar degradation (Huang et al., 2013). The PM-localized ubiquitin E3 ligase NITROGEN LIMITATION ADAPTATION (NLA) participates in the ubiquitination-mediated and clathrin-dependent endocytosis of PHT1s when Pi is replete (Lin *et al.*, 2013; Park *et al.*, 2014).

The ER is the start site where newly synthesized PHT1s travel towards the PM. The

79 ER-to-Golgi transport of PHT1s relies on the coat protein complex II (COPII)-mediated
80 vesicles or carriers (Bayle et al., 2011). However, it remains unknown how diverse
81 membrane cargoes associated with Pi starvation are transported in the late secretory
82 pathway and whether post-translational modification events regulate their packaging into
83 COPII vesicles. The formation of COPII vesicles is a multi-step process that involves the
84 recruitment of five core cytosolic factors, SAR1, SEC23, SEC24, SEC13, and SEC31, to
85 the ER exit sites (ERES) (Barlowe and Miller, 2013; Kurokawa and Nakano, 2018). In
86 particular, incorporation of multi-spanning transmembrane (TM) proteins into COPII
87 vesicles in the budding yeast *Saccharomyces cerevisiae* requires dual binding with the
88 COPII coat subunit Sec24 and the ER cargo receptor Erv14 (Powers and Barlowe, 1998;
89 Harmel et al., 2012; Pagant et al., 2015). The role of Erv14 in COPII coupling is likely
90 due to its function as a membrane chaperone, which exposes the sorting signals of Erv14
91 clients for their interaction with Sec24 and efficient capture into COPII vesicles
92 (Dancourt and Barlowe, 2010; Pagant et al., 2015). Loss of the fungal Erv14
93 compromised the targeting of several transporters destined for the late secretory
94 compartments, thus resulting in mis-regulating numerous cellular functions (Powers and
95 Barlowe, 1998; Nakanishi et al., 2007; Pagant et al., 2015; Zimmermannová et al., 2019;
96 Zheng et al., 2023). The *Drosophila* Cornichon (Cni), like its yeast homolog Erv14, was
97 shown to recruit the epidermal growth factor (EGF)-like ligand Gurken into COPII
98 vesicles (Roth *et al.*, 1995; Bökel *et al.*, 2006). Without Cni, the ER export and secretion
99 of Gurken are disrupted (Bökel et al., 2006).
100 Similarly, the plant CORNICHON HOMOLOG proteins (CNIHs) act as the ER cargo
101 receptors for various ion and metabolite transporters (Rosas-Santiago *et al.*, 2015;
102 Wudick *et al.*, 2018; Wei *et al.*, 2023; Yáñez-Domínguez *et al.*, 2023). The *Arabidopsis*
103 *thaliana* CNIHs (*At*CNIH1–5) have three putative transmembrane domains (TMDs), with
104 the N terminus facing the cytosol, the C terminus facing the ER lumen, and at least four
105 functional motifs (Wudick *et al.*, 2018; Chiu *et al.*, 2024). The cornichon motif is located
106 between the first and second TMD of Erv14 and is well-conserved across all *At*CNIHs
107 (Wudick *et al.*, 2018). The FLN motif, known as a cargo-binding site in the second TMD
108 of Erv14 (Pagant et al., 2015), and the cytosolic IFRTL motif, located between the second
109 and third TMD of Erv14 and interacting with Sec24 (Powers and Barlowe, 2002), are also
110 present in *At*CNIH2–4 with several residues changed. Lastly, the C-terminal acidic motif,

111 only found in plants and fungi, is required for Erv14 to assist the PM targeting of the
112 yeast Nha1, Pdr12, and Qdr2, as well as for the rice *Oryza sativa* CNIH1 (*Os*CNIH1) to
113 aid the Golgi targeting of *Os*HKT1;3 (Rosas-Santiago et al., 2017).

114 We recently uncovered that *AtCNIH5* is a Pi starvation-induced (PSI) gene
115 preferentially expressed in the outer layers of the root above the apical meristem (Chiu et
116 al., 2024). *At*CNIH5 localizes to the ER and is closely associated with the
117 *At*SAR1A/*At*SEC16A/*At*SEC24A-labeled ERES (Chiu et al., 2024). The T-DNA
118 knockout mutant of *AtCNIH5* exhibited a lower abundance of *At*PHT1;1/2/3 and
119 *At*PHT1;4 in the root microsomal fractions, with reduced shoot Pi levels and shoot-to-
120 root distribution of ^{32}P under Pi sufficiency and decreased ^{32}P uptake under Pi deficiency
121 (Chiu et al., 2024). The fluorescent protein tagged-*At*PHT1;1 in the Pi-limited root of
122 *cnih5* was, in part, retained intracellularly in the root hair and in the epidermis within the
123 transition/elongation zones (Chiu et al., 2024). Consistently, the fluorescence intensities
124 of the *At*PHT1;1 fusion proteins diminished at the PM of the aforementioned root cells
125 compared to the wild-type (WT) control (Chiu et al., 2024). These findings suggested a
126 potential role for *At*CNIH5 in facilitating the transport of *At*PHT1s from the ER to the
127 Golgi.

128 Intriguingly, phenotypes such as shorter root hairs and higher lateral root densities
129 were also observed for *cnih5* (Chiu et al., 2024). Considering that *At*CNIH5 may serve as
130 a cargo receptor for a broader range of membrane proteins beyond *At*PHT1s and that
131 inefficient ER export of membrane cargoes in *cnih5* may cause their intracellular
132 retention and eventual degradation due to the protein quality control, we reasoned that
133 the steady-state levels of membrane cargoes of *At*CNIH5 would be reduced in *cnih5*. To
134 identify potential cargoes of *At*CNIH5 associated with Pi starvation, we employed
135 isobaric tags for relative and absolute quantification (iTRAQ)-based membrane
136 proteomics. Because membrane proteins are highly hydrophobic and have low
137 abundance, isolation of microsomal proteins (MPs) enriched for PM, ER, Golgi, vacuolar
138 membranes, and endosomal vesicles is challenging (Wang and Liang, 2012).
139 Conventionally, MPs are solubilized with sodium dodecyl sulfate (SDS) or other anionic
140 detergents. However, SDS affects the performance of liquid chromatography-tandem
141 mass spectrometry (LC–MS/MS), and removing SDS before mass spectrometry analysis
142 results in an unavoidable loss of MPs (Wang and Liang, 2012). A study using the rice

143 leaf as a model system demonstrated that the microcentrifugation-based microsomal
144 protein extraction (MME) method is effective for downstream label-free quantitative
145 proteome analysis, requiring neither a large amount of plant material nor
146 ultracentrifugation to enrich PM proteins (Nguyen et al., 2021). The authors also applied
147 the UV-cleavable and mass spectrometry-compatible surfactant 4-
148 hexylphenylazosulfonate (Azo) (Brown *et al.*, 2019; Brown *et al.*, 2020) to minimize
149 protein losses by omitting the SDS detergent wash step. Their results revealed several
150 advantages of Azo over SDS in solubilizing the MPs, including a higher number and
151 abundance of MPs (Nguyen et al., 2021). In this study, we modified the Azo-solubilized
152 MME method to isolate root MPs from Pi-limited *Arabidopsis* WT and *cnih5* for iTRAQ
153 proteomic analysis. We targeted our research to root MPs to reduce sample complexity,
154 thus increasing the possibility of identifying functionally relevant protein changes in
155 *cnih5*. Additionally, the membrane proteome analysis of Pi-limited roots provides
156 valuable insights into the physiological role of *At*CNIH5. It also provides the first
157 database of the membrane proteome for Pi-limited root biology research (Zhou et al.,
158 2022).

159 With this approach, we identified 4,317 proteins in the Pi-limited WT and *cnih5* roots,
160 in which 1,231 proteins (28.5%) have at least one TM helix. Of the differentially
161 expressed proteins (DEPs) in *cnih5*, 372 and 106 proteins are upregulated and
162 downregulated with ratios ≥ 1.25 or ≤ 0.75, respectively. Consistent with the primary role
163 of *At*CNIH5 in the ER export of membrane cargoes, the Gene Ontology (GO) and Kyoto
164 Encyclopedia of Genes and Genomes (KEGG) pathway enrichment analyses supported
165 that the impairment of *At*CNIH5 leads to alterations in vesicular trafficking and suggested
166 a close association of the downregulated proteins with protein export and localization.
167 We also found that several transmembrane enzymes involved in the biosynthesis or
168 modification of cell wall polysaccharides, very long-chain fatty acids (VLCFAs), and
169 their derivative extracellular aliphatic compounds, such as cutin, suberin, and wax, are
170 downregulated in Pi-limited *cnih5* roots. Using the yeast split-ubiquitin system (SUS) and
171 the *in-planta* tripartite split-GFP assay, we confirmed the interaction of *At*CNIH5 with
172 various potential membrane cargoes, including a number of transporters such as
173 *At*PHT1s, *At*OCT1, *At*URGT6, *At*DTX21, and *At*DTX35. We generated a series of C-
174 terminally truncated forms of *At*CNIH5 to find out which motif of *At*CNIH5 interacts

175 with *At*PHT1;1. *At*CNIH5 1–26, which contains only the first TMD, is sufficient for
176 localization to the ER in agro-infiltrated *Nicotiana benthamiana* (*N. benthamiana*) leaves
177 and for interacting with *At*PHT1;1 in plant and yeast cells. Interestingly, the C-terminal
178 tail of *At*CNIH5, which carries one aspartic acid residue, is required for interaction with
179 *At*OCT1 but not with *At*PHT1;1 or *At*DTX21. Therefore, unlike the fungal and rice
180 CNIHs interacting with their cognate cargoes through the C-terminal acidic motif,
181 *At*CNIH5 employs a distinct mechanism to select *At*PHT1;1 as its cargo. Importantly,
182 introducing the *At*CNIH5 genomic-GFP translation fusion to complement the *cnih5*
183 mutant boosted plant growth under suboptimal Pi supply, suggesting that *At*CNIH5 acts
184 as a hub to facilitate the ER export of specific membrane cargoes associated with Pi
185 starvation to improve plant fitness.
186
187 **Results**
188 **Azo-solubilized microcentrifugation-based microsomal protein extraction (MME)**
189 **of *Arabidopsis* roots**
190 Because the application of Azo promoted fast and reproducible tryptic digestion for
191 quantitative proteomics (Brown et al., 2020), we replaced the mass spectrometry-
192 incompatible surfactant SDS with Azo and established an efficient workflow of MPs
193 extraction for quantitative proteomic analysis of *Arabidopsis* roots (**Fig. 1A**). To ensure
194 that the Azo wash step can be skipped prior to mass spectrometry analysis, we tested the
195 time-course effect of UV irradiation on Azo breakdown (Brown et al., 2019). Within 40
196 min of UV illumination, 1% Azo in 100 mM triethylammonium bicarbonate (TEABC)
197 almost wholly degraded (**Fig. 1B**). After tryptic digestion and Azo degradation, small
198 aliquots of four samples—two biological replicates each for WT and *cnih5*—were pre-
199 analyzed in a single one-dimensional (1D)–LC–MS/MS run. A summary of the label-free
200 proteomic analysis for quality check is shown in Fig. S1A. We used multiple marker
201 abundance profiling (MMAP) (Hooper et al., 2016) to estimate the relative abundance of
202 organelles in the MPs samples. The results suggested that the modified Azo-solubilized
203 MME method greatly removed proteins targeted to the plastid, nucleus, and extracellular
204 space while enriching proteins targeted to the mitochondria, ER, Golgi, PM, and vacuole
205 (Fig. S1B, C). To further evaluate this modified MME method, we examined the
206 abundance of the well-established root MPs, including the PM-targeted *At*NRT2.1

207 (Chopin et al., 2007), *At*PHT1;1/2/3 and *At*PHT1;4, the Golgi-localized *At*PHO1 (Arpat
208 *et al.*, 2012; Liu *et al.*, 2012), and the ER-resident *At*PHF1. While the amount of NRT2.1
209 declined under Pi starvation and showed no differences between WT and *cnih5*, the levels
210 of *At*PHT1;1/2/3, *At*PHT1;4, *At*PHF1, and *At*PHO1 were upregulated following Pi
211 deprivation (**Fig. 2A**), as previously reported. Importantly, the abundance of
212 *At*PHT1;1/2/3 and *At*PHT1;4 decreased in *cnih5* compared to the WT controls, regardless
213 of Pi availability, whereas *At*PHF1 proteins were more abundant in *cnih5* than in WT
214 (**Fig. 2A**), which aligns with our recent immunoblot results obtained from commercial
215 membrane protein extraction or total protein extraction methods (Chiu et al., 2024).
216 Collectively, these data justified the suitability of the modified Azo-solubilized MME
217 method for enriching root MPs.
218
219 **Upregulation of *At*CNIH5 in the root during Pi starvation and in the Pi**
220 **overaccumulator *pho2* under Pi sufficiency**
221 Since *At*CNIH5 was not identified in our small-scale label-free proteomic analysis, we
222 raised a specific polyclonal antibody to detect the abundance of *At*CNIH5 in the root MPs.
223 This antibody recognized a band in the Pi-limited roots of WT seedlings at ∼15 kDa that
224 was absent in *cnih5* (**Fig. 2B**). In agreement with the finding that low Pi induces the gene
225 expression of *AtCNIH5* (Chiu et al., 2024), the protein amount of *At*CNIH5 was also
226 elevated during Pi starvation (**Fig. 2B**), suggesting that *AtCNIH5* is upregulated by Pi
227 starvation at the transcript and protein level. Of note, under Pi sufficiency, *At*CNIH5
228 modestly accumulated in the root of *pho2* relative to the WT control (**Fig. 2B**). This
229 increase was recapitulated by two other different MPs extraction methods (**Fig. 2B**),
230 validating the previous membrane proteomic analysis showing that the protein level of
231 *At*CNIH5 significantly increased in the Pi-replete root of *pho2* relative to the WT (Huang
232 et al., 2013). These results suggest that *At*CNIH5 expression is induced to meet the
233 increased demand for ER export of *At*PHT1s, supporting the genetic evidence from our
234 side-by-side study, which shows that loss of *AtCNIH5* alleviates the Pi toxicity of *pho2*
235 (Chiu et al., 2024).
236
237 **Dysfunction of *At*CNIH5 alters vesicular trafficking, acyl-lipid metabolism, and cell**
238 **wall composition under Pi limitation**

239 After labeling the tryptic-digested peptides with iTRAQ reagents, we mixed and
240 separated them using two-dimensional high-performance liquid chromatography (2D–
241 HPLC). Each fraction was diluted and trapped onto a reverse-phase column for
242 separation, followed by Orbitrap mass spectrometry. By combining the total proteins of
243 the four samples, we identified 32,812 peptides and 21,433 unique peptides that matched
244 with 4,317 proteins with confidence (criteria described in Materials and Methods),
245 resulting in an average sequence coverage of 17.8% (Table S1). About 99.3% of the
246 identified proteins were shared across the four samples (Table S1), indicating that our
247 proteomic data were unbiased, as nearly all proteins within the detection range could be
248 identified. The proteins containing TM helices were predicted or annotated by
249 DeepTMHMM and UniProtKB (**Fig. 3A)** (Krogh *et al.*, 2001; Hallgren *et al.*, 2022; The
250 UniProt Consortium, 2023). The 1,231 identified proteins (28.5%) have at least one TM
251 helix and thus are integral membrane proteins (**Fig. 3A**). The subcellular localizations of
252 the 4,317 identified proteins based on SUBA5 (Hooper et al., 2016) showed that 7.8%
253 localize to the ER, 10.1% to the Golgi, 4.4% to the vacuole, and 16.2% to the PM (**Fig.
254 3B**). Consequently, about 37.3% (1,609) and 21.2% (915) represent MPs and integral
255 MPs, respectively (**Fig. 3A**), while 19.3% of the 915 integral MPs localized to the ER,
256 15.7% to the Golgi, 9.7% to the vacuole, and 31.7% to the PM (**Fig. 3C**). The general and
257 detailed descriptions of proteomics data, including the summary of proteomic analysis,
258 protein scores and mass, annotation, and quantification for the identified proteins, are
259 listed in Table S1.
260 The 4,317 identified proteins were subjected to GO enrichment analysis by ShinyGO
261 0.82 (Ge et al., 2019). Only the top significant GO terms (FDR adj. p-value < 0.05) were
262 shown according to the ranking of fold enrichment. The top terms are nucleoside-
263 triphosphatase (NTPase) activity, pyrophosphatase (PPase) activity, and mRNA binding
264 in the molecular function (MF) category; intracellular transport, protein transport, and
265 establishment of protein localization in the biological process (BP) category; plant-type
266 vacuole and cell-cell junction in the cellular component (CC) category (Table S1 and Fig.
267 S2). These results indicated that Pi depletion significantly impacts NTP- and PPi-
268 dependent cellular activities required for endomembrane trafficking.
269 In comparison to the previous finding that analyzed quantitative total protein profiling
270 in Pi-deficient versus Pi-sufficient *Arabidopsis* roots (Lan et al., 2012), we observed that

271 among the 209 significantly up-regulated proteins in their datasets (Pi-deficient/Pi-
272 sufficient plants ratio of ≥ 1.29), 57 proteins—13 of which are integral MPs—overlapped
273 with our identified 4,317 proteins in Pi-limited roots (Table S1). This overlap accounts
274 for 27.3% of the PSI proteins in their study. By contrast, we identified an additional 902
275 integral MPs (Table S1), indicating that enriching MPs for proteomics greatly expands
276 the inventory of identified proteins implicated in Pi starvation responses.

277 Consistent with the immunoblot results (**Fig. 2A**), our proteomic data showed
278 decreased protein abundance of several *At*PHT1 members and increased protein
279 abundance of *At*PHF1 in Pi-limited root of *cnih5* compared to WT (**Table 1**). Specifically,
280 we detected downregulation of *At*PHT1;2, *At*PHT1;3, and *At*PHT1;4 in at least three
281 ratios (fold changes), with at least one ratio having FDR adj. *p*-value ≤ 0.05. Although
282 not statistically significant, the downregulation of *At*PHT1;1 and *At*PHT1;5, along with
283 the upregulation of *At*PHF1, displayed a consistent trend across four ratios. In contrast,
284 *At*PHT1;9 was upregulated in the Pi-limited root of *cnih5* (**Table 1**). Volcano plots
285 summarized the results from the four comparisons and highlighted the differentially
286 expressed *At*PHT1 members and *At*PHF1 (**Fig. 3D**).

287 Although *At*PHT1;1 is a *bona fide* membrane cargo of *cnih5* (Chiu et al., 2024), we
288 noticed that the ratios of quantified *At*PHT1s varied across the four comparisons (**Table
289 1**), likely due to the limited number of biological replicates. To generate a more
290 comprehensive list of DEPs for GO enrichment analysis, we adjusted the stringency of
291 the protein profile comparisons by defining DEPs as those with at least two ratios ≥ 1.25
292 or ≤ 0.75 without applying FDR-adjusted *p*-value cutoffs. We also excluded candidates
293 showing any opposite trends (≥ 1.25 or ≤ 0.75) across the four comparisons. As a result,
294 we identified 372 upregulated proteins and 106 downregulated proteins in *cnih5* (Table
295 S2). The GO enrichment analysis (FDR adj. *p*-value < 0.05) for the 372 upregulated
296 proteins revealed that the top terms include copper ion binding, mRNA binding, and
297 oxidoreductase activity in the MF category; sulfur compound biosynthetic process and
298 purine nucleotide metabolic process in the BP category; cell-cell junction and
299 plasmodesma in the CC category (Table S2 and Fig. S3A). The KEGG pathway
300 enrichment analysis indicated that the most significantly enriched pathways are ascorbate
301 and aldarate metabolism, as well as fructose and mannose metabolism (Fig. S3B). These
302 results indicated that the upregulated proteins in the Pi-limited *cnih5* roots encode several

303 enzymes involved in carbohydrate metabolic pathways, which may help protect plant
304 cells from oxidative damage, likely reflecting compensatory mechanisms for the loss of
305 *At*CNIH5. Interestingly, when focusing on the 51 upregulated integral MPs, we found
306 significant GO terms related to transporter activities (Fig. S3C) and KEGG analyses
307 revealed a strong association with SNARE-mediated vesicular transport (Fig. S3D).
308 For GO enrichment analysis of the 106 downregulated proteins, the most significant
309 GO terms within the MF category include 7S RNA binding and fatty acid elongase
310 activity (**Fig. 4A** and Fig. S4A); within the BP categories, the top terms are protein
311 transport, cellular macromolecule localization, and establishment of protein localization
312 (**Fig. 4B** and Fig. S4A); within the CC categories, the enriched terms are the AP-type
313 membrane coat adaptor complex (**Fig. 4C** and Fig. S4A). These results can be attributed
314 to the downregulation of membrane protein localization, Golgi-associated clathrin
315 assembly, and the signal recognition particle (SRP) subunits that mediate co-translational
316 membrane protein targeting (Table S2). We thus surmised that the loss of *At*CNIH5
317 triggers negative feedback regulation of protein translation and the formation of clathrin-
318 coated vesicles, thereby reducing futile coated-vesicle assembly and preventing the toxic
319 accumulation of *At*CNIH5-dependent cargoes in the ER. Furthermore, the KEGG
320 enrichment analysis indicated that the downregulated proteins were associated with
321 processes such as fatty acid elongation, protein export, cutin/suberin/wax biosynthesis,
322 and modification of cell wall polysaccharides (Fig. S4B). Overall, the downregulated
323 proteins in Pi-limited *cnih5* roots are linked to changes in vesicular trafficking, acyl lipid
324 metabolism, and cell wall composition. Because of the limited availability of other
325 antibodies for further validation of our quantitative proteomic data by immunoblotting,
326 we conducted an additional label-free membrane proteomics on Pi-limited roots of WT
327 and *cnih5* across three biological replicates. Label-free proteomics without fractionation
328 yielded a dataset of 2035 identified proteins, which is smaller than our iTRAQ-based
329 dataset (Table S1). Nonetheless, we found an overlap of 29 proteins between the label-
330 free dataset and the iTRAQ-label downregulated proteins in Pi-limited *cnih5* roots (Table
331 S1) and validated that *At*PHT1;1, *At*PHT1;2, *At*PHT1;3, *At*PHT1;4, *At*EXPA17,
332 *At*GXM2, *At*AAP19-1, and *At*GAE1 showed a similar trend of downregulation
333 (normalized ratios $\leq$ 0.82; Table S3), supporting that these proteins are truly
334 downregulated in Pi-limited *cnih5* roots.

335

336 **Analysis of protein–protein interaction between *At*CNIH5 and its potential**
337 **membrane cargoes**

338 Considering that potential cargoes of *At*CNIH5 are downregulated integral MPs in
339 *cnih5*, we narrowed the number of candidates to 31 (**Table 2**). This list is over-represented
340 with three hypersensitive response-like lesion-inducing protein (HRLI)-like proteins
341 (AT3G23175, AT3G23190, and AT4G14420), two *β*-ketoacyl-CoA synthases (*At*KCS2
342 and *At*KCS20), and two *At*PHT1 members (*At*PHT1;1 and *At*PHT1;3) (**Table 2**).
343 Although *At*HRLI-like proteins have not been functionally characterized, the *N.*
344 *benthamiana Nb*HRLI4 conferred salicylic acid-mediated resistance to turnip mosaic
345 virus (TuMV) (Wu et al., 2021). *AtKCS* genes encode 3-ketoacyl-CoA synthases, which
346 catalyze the rate-limiting condensation step of VLCFAs biosynthesis (Evenson and Post-
347 Beittenmiller, 1995). *AtKCS2* and *AtKCS20* are highly expressed in the root endodermis
348 and redundant in root suberin biosynthesis (Lee et al., 2009). Two alcohol-forming fatty
349 acyl-CoA reductases, *At*FAR3/CER4 and *At*FAR5, are also downregulated and over-
350 represented in the KEGG pathway of cutin, suberin, and wax biosynthesis (Fig. S4B,
351 Table S2), suggesting that the biosynthesis of VLCFAs and their derivative extracellular
352 aliphatic compounds is mis-regulated in the Pi-limited roots of *cnih5*. Nevertheless,
353 *At*HRLI-like and *At*KCS proteins localize to the ER, so their downregulation may be a
354 secondary effect of *At*CNIH5 impairment.

355 Next, we selected a subset of potential membrane cargoes based on the following two
356 criteria (highlighted in gray in **Table 2**) to test their interaction with *At*CNIH5: (1) a TM
357 protein located in post-ER compartments of the secretory pathway and (2) having four
358 ratios ≤ 0.75 or at least two ratios ≤ 0.75 with at least one ratio showing FDR adj. *p*-value
359 ≤ 0.05. We recently demonstrated that *At*CNIH5 interacts with *At*PHT1;1 and *At*PHT1;4
360 (Chiu et al., 2024). In this study, we further showed that *At*CNIH5 interacts with
361 *At*PHT1;2, *At*PHT1;5, *At*PHT1;7, and *At*PHT1;9 in the yeast SUS (**Fig. 5A**), suggesting
362 that *At*CNIH5 recognizes conserved motifs among *At*PHT1 members. In addition, we
363 confirmed the interaction of *At*CNIH5 with the PM-localized receptor-like kinase
364 *At*LRK10L-1.1, nucleotide exchange factor *At*SOS, and organic cation/carnitine
365 transporter *At*OCT1, the Golgi-localized nucleotide sugar transporters *At*URGT6 and
366 glucuronoxylan 4-O-methyltransferase *At*GXM2, and the tonoplast (TP)-localized

367 detoxification efflux carriers *At*DTX21 and *At*DTX35 (**Fig. 5B)**. Similar results were also
368 obtained when the *At*SOS, *At*OCT1, *At*URGT6, *At*DTX21, and *At*DTX35 expression
369 constructs were generated with different fusion orientations (Fig. S5).
370 *AtOCT1* is a PSI gene (Liu et al., 2016) and its expression is restricted to the
371 vasculature of the root, as well as at sites of lateral root formation (Lelandais-Brière et al.,
372 2007), suggesting that the interaction of *At*CNIH5 and *At*OCT1 is likely to occur in the
373 vascular tissues. Both *At*URGT6 and *At*GXM2 are cell wall-modifying enzymes.
374 *At*URGT6 is involved in the biosynthesis of rhamnogalacturonan-I (RG-I), a component
375 of pectin found in mucilage and various types of plant cell walls (Saez-Aguayo et al.,
376 2020). *At*GXM2 is a methyltransferase that catalyzes 4-O-methylation of glucuronic acid
377 (GlcA) side chains on the hemicellulose xylan (Lee *et al.*, 2012; Urbanowicz *et al.*, 2012;
378 Yuan *et al.*, 2014). Notably, *AtGXM2* is upregulated during Pi starvation (Liu et al., 2016)
379 and is preferentially expressed in the root hair (Salazar-Henao and Schmidt, 2016).
380 *At*DTX21 and *At*DTX35 belong to the multidrug and toxic compound extrusion (MATE)-
381 type transporter superfamily. *At*DTX35 is also low Pi-responsive (Liu et al., 2016) and
382 functions as a turgor-regulating chloride channel associated with root hair elongation
383 (Zhang et al., 2017). Therefore, *At*CNIH5 may modulate cell wall elasticity and root hair
384 growth, which is consistent with decreased root hair length in *cnih5* (Chiu et al., 2024).
385 To explore other potential membrane cargoes of *At*CNIH5 that may be missing in our
386 iTRAQ-based proteomic data, we set out in parallel to find root PSI genes encoding
387 transporters that are co-regulated with *AtCNIH5*. We queried the RNA-seq dataset from
388 *Arabidopsis* seedlings subjected to Pi deprivation (P0: Pi-sufficiency; P1: one day of Pi
389 deprivation; P3: three days of Pi deprivation) (Liu et al., 2016). Genes with expression
390 levels less than 1 RPKM were excluded. We filtered root PSI genes that displayed an
391 expression pattern similar to that of *AtCNIH5* based on (1) the $\log_2$FC ≥ 0.5 (P1/P0), (2)
392 the $\log_2$FC ≥ 1 (P3/P0), and (3) the difference of $\log_2$FC ≥ 0.5 (P3/P0−P1/P0). Such
393 cutoffs were applied to root PSI genes because the agriGO enrichment analysis (Tian et
394 al., 2017) yielded a satisfactory list for further investigation, including nearly all *At*PHT1s
395 and more than ten other genes encoding transporters (Table S4). Among the list, the PM-
396 localized *At*OCT1, potassium transporter *At*HAK5, sulfate transporter *At*SULTR1;3, and
397 the TP-localized Pi transporter *At*VPE1 were selected for testing interaction with
398 *At*CNIH5 based on the tripartite split-GFP association in agro-infiltrated *N. benthamiana*

399 leaves (Liu *et al.*, 2018; Liu, 2021). We also included *At*SOS, *At*URGT6, *At*DTX21, and
400 *At*DTX35 for testing, but excluded *At*LRK10L-1.1 and *At*GXM2 due to their similar
401 membrane topology to *At*CNIH5 and the inability to find any agrobacteria transformants
402 carrying the *At*LRK10L-1.1 construct. The S10-tagged *At*CNIH5 (S10-*At*CNIH5) and the
403 S11-tagged fusion protein of interest correctly reached their subcellular destinations,
404 except that *At*SOS-S11 and *At*SULTR1;3-S11 were retained in the ER (**Fig. 6A**).
405 Compared to the recently reported positive control *At*PHT1;1-S11 (Chiu et al., 2024) and
406 the negative control 3xHA-S11, S10-*At*CNIH5 also interacted with *At*OCT1-S11, *At*SOS-
407 S11, *At*URGT6-S11, *At*DTX21-S11, and *At*DTX35-S11, yielding fluorescence signals as
408 a result of GFP complementation; however, S10-*At*CNIH5 failed to interact with
409 *At*HAK5-S11, *At*SULTR1;3-S11, and *At*VPE1-S11 (**Fig. 6B**). Taken together, our
410 membrane proteomics successfully identified several potential cargoes of *At*CNIH5,
411 including *At*PHT1s.
412
413 **The C-terminal acidic residue of *At*CNIH5 is not required to interact with *At*PHT1;1**
414 As *At*PHT1s were prominent cargoes of *At*CNIH5, we are interested in determining
415 which motif of *At*CNIH5 interacts with *At*PHT1;1. On the basis of sequence similarity,
416 we refer to the putative FLN motif in the second TMD of *At*CNIHs as the YLC motif and
417 the putative cytosolic IFRTL motif as the IFNNL motif (Fig. S6). Notably, *At*CNIH5 has
418 putative YLC and IFNNL motifs with several residues changed and a shorter C-terminal
419 putative acidic motif with only one aspartic acid residue (Fig. S6). We designed a series
420 of C-terminally truncated forms of *At*CNIH5. For an unknown reason, we failed to obtain
421 the clone expressing *At*CNIH5 1–102. Therefore, we only tested the interaction of
422 *At*PHT1;1 with *At*CNIH5 1–26, *At*CNIH5 1–49, *At*CNIH5 1–92, and *At*CNIH5 1–132 in
423 the yeast SUS (**Fig. 7A**). *At*CNIH5 1–26, which contains only the first TMD, is sufficient
424 to interact with *At*PHT1;1, while *At*CNIH5 1–132, which has the last three amino acids
425 deleted, including the C-terminal aspartic acid, still interacts with *At*PHT1;1 (**Fig. 7B**).
426 We also examined whether the truncated variants *At*CNIH5 1–26 and *At*CNIH5 1–132
427 interact with *At*PHT1;1 in plant cells. Both the *At*CNIH5 truncated variants localized to
428 the ER (**Fig. 7C**) and interacted with *At*PHT1;1 (**Fig. 7D**). Interestingly, *At*CNIH5 1–132
429 also interacted with *At*DTX21 but not with *At*OCT1 (**Fig. 7C**). Therefore, the C-terminal
430 acidic residue of *At*CNIH5 is required for interaction with *At*OCT1 but not with *At*PHT1;1

431 or *At*DTX21. As such, *At*CNIH5 interacts with *At*PHT1;1, and likely the other *At*PHT1s,
432 through a distinct mechanism that differs from those used by the fungal and rice CNIHs
433 for their cognate cargoes.
434
435 **Increasing *in-situ At*CNIH5 expression/activity enhances plant growth**
436 Since loss of *At*CNIH5 leads to decreased abundance of *At*PHT1s and other membrane
437 cargoes (**Table 2**), it was imperative to assess whether overexpression of *At*CNIH5 can
438 improve plant fitness. We found that ectopic expression of RFP-*At*CNIH5 driven by the
439 cauliflower mosaic virus (CaMV) 35S promoter resulted in distorted root morphology
440 (Fig. S7). This aberrant structure was likely caused by ER deformation, a phenomenon
441 associated with Erv14 overexpression in budding yeast (Lagunas-Gomez et al., 2023).
442 Intriguingly, we recently showed that several transgenic lines expressing the genomic
443 GFP-*AtCNIH5* fragment (*AtCNIH5pro*: GFP-*AtCNIH5*) in the *cnih5* background restored
444 the abundance of *At*PHT1;1/2/3 to levels comparable to or higher than WT during Pi
445 deficiency (Chiu et al., 2024). Under Pi sufficiency, these transgenic lines grew larger
446 and showed WT-like shoot Pi content *per plant,* but had lower shoot Pi levels (Chiu et
447 al., 2024). Therefore, we systematically examined the growth of these lines under
448 different Pi regimes. Under Pi sufficiency and modest Pi deficiency—either three days of
449 Pi deprivation (0 μM Pi) or eleven days of suboptimal Pi supply (50 μM Pi), these plants
450 exhibited higher shoot and/or root fresh weight than the WT and *cnih5* plants (**Fig. 8**). In
451 contrast, under more severe Pi deficiency—eleven days of Pi deprivation (0 μM Pi), none
452 of these lines had a larger shoot size than WT (**Fig. 8**). Although we could detect GFP-
453 *AtCNIH5* proteins in the Pi-limited root of *AtCNIH5pro*: GFP-*AtCNIH5/cnih5* plants, it
454 is technically difficult to discern whether GFP-*AtCNIH5* proteins were more abundant
455 than the endogenous *At*CNIH5 in WT (Fig. S8). Nonetheless, the higher biomass of these
456 transgenic plants is likely due to increased expression or activity of GFP-*AtCNIH5*, along
457 with additional membrane cargoes beyond *At*PHT1s, leading to more efficient
458 assimilation of acquired Pi. We inferred that a subtle increase in *in-situ* rather than ectopic
459 expression/activity of GFP-*AtCNIH5* suffices to activate downstream effectors of
460 *At*CNIH5, thereby boosting plant growth.
461
462 **Discussion**

463 CNIHs are the eukaryotic conserved cargo receptors that cycle between the ER and
464 the early Golgi to select membrane proteins for incorporation into COPII vesicles. In this
465 study, we aimed to identify potential membrane cargoes of low Pi-induced *At*CNIH5
466 through iTRAQ-based proteomic analysis, while also providing the first comprehensive
467 membrane proteome for *Arabidopsis* roots subjected to Pi deprivation (Zhou et al., 2022).
468 Given that our iTRAQ-based proteomic analysis did not include Pi-sufficient WT and
469 *cnih5* samples, we sought to evaluate whether the identified potential membrane cargoes
470 of *At*CNIH5 are PSI proteins. To address this, we examined the overlap between the
471 proteins we identified in the Pi-limited roots and the root PSI genes in the RNA-seq
472 dataset (P3/P0, FC > 1.5; Liu et al., 2016). We found minimal overlap, at only 5.8%,
473 between the 4,317 identified proteins and the root PSI genes (Table S1). This finding
474 aligns with the previous study, which indicated a weak correlation between transcript and
475 protein changes following Pi deficiency in *Arabidopsis* roots (Lan et al., 2012). Still, of
476 our identified integral MPs in the Pi-limited roots, 7.8% (4 out of 51) of the upregulated
477 and 32.3% (10 out of 31) of the downregulated proteins in *cnih5* were classified as root
478 PSI genes (Table S5). These results indicated that, compared with PSI genes within the
479 4,317 identified proteins, PSI genes are enriched 5.6-fold among the downregulated
480 integral MPs in Pi-limited *cnih5* root (Table S5). Therefore, the *At*CNIH5-dependent
481 membrane cargoes we identified are mainly associated with Pi starvation.
482 When expressed in the yeast heterologous expression system, *At*CNIH5 interacted not
483 only with the two major Pi transporters, *At*PHT1;1 and *At*PHT1;4 (Chiu et al., 2024), but
484 also with *At*PHT1;2, *At*PHT1;5, *At*PHT1;7, and *At*PHT1;9 (**Fig. 5A**), supporting that
485 *At*PHT1s are the prominent membrane cargoes of *At*CNIH5. This was not surprising
486 because the amino acid sequences of *At*PHT1s share over 47.4% identity. It has been
487 shown that the yeast and rice CNIHs used the C-terminal acidic motif to interact with
488 their cognate cargoes (Rosas-Santiago et al., 2017). However, a recent study revealed that
489 the cargo binding motif of the pumpkin *Cm*CNIH1 may reside in the N-terminal rather
490 than the C-terminal region (Wei et al., 2023). This agreed with our results for the
491 interaction between *At*CNIH5 and *At*PHT1;1 (**Fig. 7B**), indicating that the first TMD of
492 *At*CNIH5 contains a motif that interacts with *At*PHT1s.
493 Besides *At*PHT1s, we identified other PM-localized membrane proteins that were
494 downregulated in Pi-limited *cnih5* roots. *At*LRK10L-1.2 is involved in ABA signaling

495 (Lim et al., 2015). The animal Son of Sevenless (SOS) proteins encode guanine
496 nucleotide exchange factors that act on the Ras subfamily of small GTPases (Bowtell et
497 al., 1992). However, the physiological role of SOS in plants remains to be studied. The
498 PSI *At*OCT1 was also identified as a cargo of *At*CNIH5. We further demonstrated that
499 the C-terminal motif of *At*CNIH5 is required for the interaction between *At*OCT1 and
500 *At*CNIH5 (**Fig. 7D**). Notably, the *oct1* mutant exhibited enhanced root branching
501 (Lelandais-Brière et al., 2007), phenocopying the higher lateral root density of *cnih5*
502 (Chiu et al., 2024). Although the heterologous expression of *At*OCT1 in yeast could
503 transport carnitine, it remains to be determined which substrate *At*OCT1 transports that
504 could negatively affect lateral root development.

505 Previous analyses of root-specific co-expression have indicated that early PSR genes
506 are involved in cell wall remodeling, highlighting the importance of this process in
507 response to Pi deficiency (Liao *et al.*, 2011; Lin *et al.*, 2011). Various Golgi-localized
508 proteins involved in plant cell wall modification, such as *At*QUL2 (AT2G03480)
509 (Mouille et al., 2007), *At*GAE1 (AT4G30440) (Mølhøj et al., 2004), *At*GAUT3
510 (AT4G38270) (Sterling et al., 2006), and *At*TMN9 (AT5G25100) (Hiroguchi et al.,
511 2021), were remarkably downregulated in the Pi-limited *cnih5* roots (**Table 2**). The
512 cytosolic UDP-glucose pyrophosphorylase 2 (UGP2, AT5G17310), which is implicated
513 in the synthesis of cell wall and callose deposition, was also downregulated in *cnih5*
514 across the four ratios (**Fig. 3D**). In contrast, the Golgi-localized hydroxyproline-O-
515 galactosyltransferase *At*GALT9 (AT1G53290), which is involved in pectin metabolism
516 (Zhang et al., 2021), was the most highly upregulated protein in Pi-limited *cnih5* roots
517 (**Fig. 3D**). We speculate that *At*CNIH5 may play a critical role in Pi starvation-triggered
518 cell wall composition changes. Nevertheless, the difference in cell wall structure between
519 WT and *cnih5* remains to be investigated.

520 The TP-localized *At*DTX21 and *At*DTX35 were identified as the potential cargoes of
521 *At*CNIH5 (**Fig. 5B**, **6B**). While *AtDTX35* is known as a PSI gene, *AtDTX21* is co-induced
522 with the type III effectors secreted by *Pseudomonas syringae* and mediates the
523 detoxification of chlorinated herbicide atrazine (de Torres-Zabala *et al.*, 2007; Ramel *et*
524 *al.*, 2007). Further studies are needed to elucidate the physiological role of *At*DTX21 and
525 *At*DTX35 in Pi starvation responses. *At*CNIH5 failed to interact with other manifest PSI
526 transporters such as *At*HAK5, *At*SULTR1;3, and *At*VPE1 (**Fig. 5B**). In fact, *At*VPE1 and

527 its paralog *At*VPE3 were identified in our proteomic analysis, while their abundance did
528 not differ between WT and *cnih5* (Table S1). This suggests that *At*CNIH5 recognizes only
529 specific PSI transporters via a mechanism yet to be elucidated.
530 In conclusion, an Azo-solubilized MME approach in conjunction with quantitative
531 proteomics was used to reveal the downregulation of *At*PHT1s and other membrane
532 proteins associated with Pi starvation in *cnih5* roots (**Fig. 9**). Our analyses validated the
533 interaction between *At*CNIH5 and several membrane proteins at post-ER compartments,
534 including *At*PHT1s, *At*OCT1, *At*URGT6, *At*DTX21, and *At*DTX35 transporters. We also
535 showed that the protein level of *At*CNIH5 increases during Pi starvation as well as in the
536 Pi-replete root of *pho2*, as a result of accommodating the increased demand for ER export
537 of *At*PHT1s. Moreover, introducing the genomic GFP-*AtCNIH5* fragment enhanced plant
538 growth across a wide range of Pi supply levels. Altogether, we propose that *At*CNIH5
539 acts as a Pi deficiency-inducible hub, facilitating the ER-to-Golgi trafficking of several
540 membrane proteins through a mechanism beyond the putative C-terminal acidic motif,
541 thereby improving plant fitness under suboptimal Pi availability.
542
543 **Materials and Methods**
544 **Plant Material and Growth Conditions**
545 Seeds of the *A. thaliana* wild-type (Columbia, Col-0) and *cnih5* (SAIL_256_B03)
546 mutants used in this study were obtained from the Arabidopsis Biological Resource
547 Center. Seeds were surface-sterilized and germinated on agar plates with one-half
548 modified Hoagland's solution containing 1% sucrose and 0.7% Bacto agar and grown in
549 the growth chamber at 22 °C with a 16-h light/8-h dark cycle. Pi-sufficient (+P; 250 μM
550 Pi) or Pi-deficient (−P; 0 μM Pi) medium containing 1.2% agar was used for vertically
551 grown plants.
552
553 **Tissue Homogenization and Microsomal Protein Preparation**
554 The roots of 11-day-old seedlings with five days of Pi starvation were harvested.
555 Approximately 100 mg of root tissue was collected for each sample and stored at −80 °C
556 for subsequent homogenization. The frozen samples were homogenized by TissueLyser
557 II (QIAGEN). The method for microsomal protein extraction was modified from a
558 previous study (Abas and Luschnig, 2010), and all steps were performed on ice or 4 °C.

559 Briefly, each sample was resuspended in 100 μl of extraction buffer (EB) containing 50
560 mM of hydroxyethyl piperazine ethane sulfonic acid (HEPES; Melford, pH 7.5), 25%
561 (w/w 0.81 M) sucrose, 5% (v/v) glycerol, 10 mM of ethylenediaminetetraacetic acid
562 (EDTA; Amresco, pH 8), 5 mM of KCl, 1 mM of dithiothreitol (DTT; Sigma), and 2×
563 protease inhibitor cocktail (P9599, Sigma). An equivalent volume (100 μl) of 5%
564 polyvinylpolypyrrolidone (PVPP; Sigma) suspension solution was used for each sample.
565 The 5% PVPP was centrifuged at 2,000×g for 1 min at room temperature (RT). The
566 precipitate was activated for 2 hours in an equivalent volume of activated solution
567 containing 100 mM HEPES, 40% (w/w, 1.37 M) sucrose, 20 mM EDTA, and 10 mM
568 KCl. The activated PVPP was centrifuged at 5,000×g for 1 min at RT, and the supernatant
569 was removed. The activated PVPP pellet was mixed with the sample suspension and stood
570 for 5 min, followed by centrifugation thrice. The first centrifugation was processed at
571 600×g for 3 min. The pellet was then re-extracted with 50 μl EB and centrifuged at 600×g
572 for 3 min. The pellet was then re-extracted with 35 μl EB and centrifuged at 2,000×g for
573 30 s. After three times centrifugation, all the supernatants were combined and centrifuged
574 again at 600×g for 3 min. The collected supernatant was diluted with an equivalent
575 volume of ddH_2O to reach a final solution concentration containing 12–13% sucrose and
576 centrifuged at 21,000×g for 90 min. The pellet was resuspended in washing buffer
577 containing 10 mM HEPES, 5 mM EDTA, 1 mM phenylmethylsulfonyl fluoride (PMSF,
578 Sigma), and 1× protease inhibitor cocktail and centrifuged at 21,000×g for 45 min. Finally,
579 the pellet was stored at −80 °C for further analysis.
580
581 **Protein Solubilization and In-Solution Digestion**
582 Microsomal protein pellets were dissolved in 1% sodium 4-hexylphenylazosulfonate (Na-
583 Azo, Excenen Pharmatech) in 100 mM triethylammonium bicarbonate (TEABC, Sigma)
584 containing 2× protease inhibitor cocktail and 1 mM PMSF. The protein yield was
585 determined by BCA assay (Pierce). For each sample, an equal amount of protein was
586 reduced with 5 mM tris-(2-carboxyethyl)-phosphine (TCEP, Sigma) at 60 °C for 30 min,
587 followed by cysteine-blocking with 10 mM methyl methanethiosulfonate (MMTS, Sigma)
588 at 25 °C for 30 min. Samples were digested with sequencing-grade modified porcine
589 trypsin (Promega) at 37 °C with shaking for 1 hour and then illuminated by 6W UV light
590 302 nm (UVP UVM-57, Analytik Jena) at 4 °C for 40 min. The digested proteins were

591 then aliquot and stored at −20 °C until use.

592

593 **Isobaric Tag for Relative and Absolute Quantitation (iTRAQ) Labeling and Peptide**
594 **Separation**

595 After trypsin digestion, 0.5 μg of peptides was subjected to 1D–LC–MS/MS without pre-
596 fractionations to identify and quantify proteins as a quality control study. On the other
597 hand, 10 μg of peptides was labeled using an iTRAQ Reagent-4 plex Multiplex Kit
598 according to the manufacturer's instructions (Applied Biosystems) for 1 hour at RT. Two
599 WT replicates were labeled with iTRAQ-114 and -115, and two *cnih5* replicates were
600 labeled with iTRAQ-116 and -117, pooled and desalted by homemade C18-microcolumn
601 (SOURCE 15RPC, GE Healthcare). The eluted peptides were dried by vacuum
602 centrifugation. The desalted peptides were loaded onto a homemade strong cation
603 exchange (SCX) column (Luna SCX 5μm, 0.5 × 120 mm) at a 2 μl/min flow rate for 60
604 min. The peptides were then fractionated to 24 fractions by eluting with 0 to 100% HPLC
605 buffer B (1 M ammonium nitrate/25% acetonitrile/0.1% formic acid) using on-line two-
606 dimensional high-performance liquid chromatography (2D-HPLC; Dionex Ultimate
607 3,000, Thermo Fisher). Each SCX fraction was diluted in-line before trapping onto a
608 reverse-phase (RP) column (Zorbax 300SB-C18, 0.3 x 5 mm; Agilent Technologies). The
609 peptides were then separated on a column (Waters BEH 1.7 μm, 100 μm I.D. × 10 cm
610 with a 15 μm tip) using a multi-step gradient of HPLC buffer C (99.9% acetonitrile/0.1%
611 formic acid) for 60 min with a flow rate of 0.3 μl/min.

612

613 **Liquid Chromatography-Tandem Mass Spectrometry (LC-MS/MS) Analysis**

614 The LC apparatus was coupled with a 2D linear ion trap mass spectrometer (LTQ-
615 Orbitrap ELITE; Thermo Fisher) operated using Xcalibur 2.2 software (Thermo Fisher).
616 The full-scan MS was performed in the Orbitrap over a range of 400 to 2,000 Da and a
617 resolution of 120,000 at m/z 400. For proteome analysis, the 10 data-dependent MS/MS
618 scan events were followed by one MS scan for the 10 most abundant precursor ions in
619 the preview MS scan. The m/z values selected for MS/MS were dynamically excluded
620 for 80 sec with a relative mass window of 1 Da. The electrospray voltage was set to 1.8
621 kV, and the capillary temperature was set to 200 °C. MS and MS2 automatic gain control
622 were set at 1,000 ms (full scan) and 300 ms (MS2 for HCD), or 3×10^6 ions (full scan)

623 and 3×10^4 ions (MS2 for HCD) for maximum accumulated time or ions.
624
625 **LC-MS Data Processing, Protein Identification and Quantification**
626 Proteome Discoverer software (version 2.3, Thermo Fisher Scientific) was used for data
627 analysis, incorporating the reporter ions quantifier node for iTRAQ quantification. The
628 MS/MS spectra were searched against the SwissProt database using the Mascot search
629 engine (Matrix Science, version 2.5). For peptide identification, a 10 ppm mass tolerance
630 was allowed for intact peptide masses and 0.2 Da for HCD fragment ions, with allowance
631 for two missed cleavages made from trypsin digestion. Variable modifications included
632 oxidized methionine, acetylation (protein N-terminal), and iTRAQ-4plex (peptide N-
633 terminal, K); methylthiolation (C) was considered a static modification. Peptide-spectrum
634 matches (PSMs) were filtered based on high confidence and Mascot search engine rank
635 1 of peptide identification, ensuring an overall false discovery rate (FDR) below 0.01.
636 Proteins with only a single peptide hit were removed. Quantitative protein data were
637 exported from Proteome Discoverer using Integration Methods of the Most Confident
638 Centroid with a 20 ppm tolerance. The data sets were analyzed by cross-comparison
639 between four samples (ratio 1, 116:114; ratio 2, 117:114; ratio 3, 116:115, and ratio 4,
640 117:115). Protein ratios in each comparison group were normalized using the median
641 ratio of each comparison group. Volcano plots of differentially expressed proteins were
642 generated using the ggplot2 (Wickham et al., 2016) and ggrepel (Slowikowski et al., 2024)
643 package in R version 4.3.1 (R Core Team, 2021). The code was written using RStudio
644 version 2023.06.2 (RStudio Team, 2020). A 1.25-fold cutoff was applied to define
645 differentially expressed proteins in each comparison group. The mass spectrometry
646 proteomics data have been deposited to the ProteomeXchange Consortium via the PRIDE
647 partner repository (Deutsch et al., 2022; Perez-Riverol et al., 2024) with the dataset
648 identifier PXD062137 and 10.6019/PXD062137.
649
650 **Protein Annotation and Interpretation**
651 Transmembrane-related information was obtained through analysis using DeepTMHMM
652 (https://dtu.biolib.com/DeepTMHMM) (Hallgren et al., 2022). Subcellular structure
653 localization was analyzed by SUBA5 (https://suba.live/) (Hooper et al., 2016). For
654 functional annotation of proteins, Gene Ontology (GO) and Kyoto Encyclopedia of Genes

655 and Genomes (KEGG) enrichment analyses were determined by ShinyGO 0.82
656 (http://bioinformatics.sdstate.edu/go/) (Ge et al., 2019), in which *p*-values were computed
657 using the hypergeometric test and multiple test correction was performed using the
658 Benjamini–Hochberg method based on an FDR cut-off of 0.05. Only pathways with a
659 minimum of 10 genes were selected. Similar pathways that share 95% of their genes and
660 50% of the words in their names were eliminated according to the setting of ShinyGO
661 0.82. Dot plots of GO enrichment analysis were generated using the ggplot2 (Wickham
662 et al., 2016) and stringr package (Wickham, 2023).
663
664 **Microsomal protein extraction for immunoblot analysis**
665 The MPs pellets were solubilized by 0.5% Azo in 25mM aqueous ammonium
666 bicarbonate, pH 7.0 (Sigma Aldrich). Alternatively, the low-speed pellet (LSP) was
667 prepared as previously described (Yoshimoto et al., 2004), and microsomal protein was
668 isolated using the Minute Plant Microsomal Membrane Extraction Kit (Invent, MM-018)
669 according to the manual instructions. A 5–30 μg of MPs from each sample was loaded
670 onto 4–12% Q-PAGE™ Bis-Tris Precast Gel (SMOBIO) or NuPAGE 4–12% Bis-Tris
671 Gels (Thermo Fisher Scientific). Gel was transferred to polyvinylidene difluoride
672 membranes (Immobilon-P Membrane or Immobilon®-PSQ Membrane; Merck).
673 Membrane was blocked with 1–2% BSA in 1× PBS solution with 0.2% Tween 20 (PBST,
674 pH 7.2) at RT for 1 h, and rinsed two times with distilled water followed by hybridization
675 with primary antibodies of *At*PHF1 (Huang et al., 2013), *At*PHO1 (Liu et al., 2012),
676 *At*NRT2.1 (AS12 2612; Agrisera), and *At*CNIH5 at RT for 2 h or at 4 °C overnight in
677 blocking solution. Polyclonal rabbit *At*CNIH5 antibody was raised against the region
678 corresponding to the amino acid residues 96 to 114 (TELYNTNKWEQKKRVYKIG) by
679 LTK BioLaboratories, Taiwan, and was affinity purified. The membrane was washed four
680 times with 1× PBST for 5 min followed by hybridization with the horseradish peroxidase–
681 conjugated secondary antibody (GTX213110-01 or GTX213111-01; GeneTex) in
682 blocking solution at RT for 1 h. After four washes in 1× PBST for 5 min and a rinse with
683 distilled water, chemiluminescent substrates (WesternBright ECL or Sirius; Advansta)
684 were applied for signal detection.
685
686 **Construct design and yeast split-ubiquitin assay**

687 For constructing the yeast expression clones, the coding sequence (CDS) of the gene of
688 interest (GOI), including *At*LRK10L-1.1, *At*GXM2, *At*SOS, *At*DTX21, *At*DTX35,
689 *At*URGT6, *At*OCT1, and the truncated *At*CNIH5 variants, was amplified by PCR, cloned
690 into the pCR8/GW/TOPO vectors and sequenced. The pCR8/GW/TOPO construct
691 containing the CDS of *AtPHT1;1* was cloned as previously reported (Huang et al., 2013).
692 The entry clones were recombined into NX32_GW (ABRC CD3-1737) or XN22_GW
693 (ABRC CD3-1735) through LR reactions, resulting in N or C-terminally fused Nub
694 fragments or into MetYC_GW (ABRC CD3-1740) through LR reactions, resulting in
695 *At*PHT1;1-PLVCub. The PLVCub-*At*CNIH5 construct was generated as recently
696 reported (Chiu et al., 2024). The Nub and PLVCub expression clones were sequentially
697 transformed into the yeast THY.AP4 strain (ABRC CD3-808; (Obrdlik et al., 2004).
698 Fresh yeast colonies picked from yeast extract peptone dextrose adenine (YPDA) medium
699 or synthetic complete (SC) medium without leucine (SC–L) were inoculated in the
700 corresponding liquid medium and incubated overnight at 30 °C with shaking at 200 rpm.
701 Overnight yeast culture was then diluted to OD_{600} = 0.2 and grew for another 4–6 h until
702 OD_{600} reached 0.4–0.6. Yeast pellet was collected by centrifugation at 2,000×g at 4 °C
703 for 10 min, washed with ddH_2O, and resuspended in Tris-EDTA/lithium acetate solution
704 (TE/LiAc, 10 mM Tris-HCl [pH 8.0], 1 mM EDTA, and 0.1 M lithium acetate). Yeast
705 transformants carrying the PLVCub-*At*CNIH5 or *At*PHT1;1-PLVCub were selected and
706 maintained on SC–L for sequential transformation with NubI (positive control), NubG
707 (negative control), and GOI-NubG or NubG-GOI. Yeast transformants carrying the Nub
708 and the PLVCub constructs were selected and maintained on SC medium without leucine
709 and tryptophan (SC–LW). For the protein–protein interaction testing, yeast cells co-
710 expressing PLVCub-*At*CNIH5 or *At*PHT1;1-CubPLV with GOI-NubG or NubG-GOI
711 were grown on synthetic media lacking leucine, tryptophan, adenine, and histidine (SC–
712 LWAH) with 500 μM methionine or on SC–LW containing 100 mg/L 5-bromo-4-chloro-
713 3-indolyl-*β*-d-galactopyranoside (X-Gal) at 30 °C for 24–36 h. Primer sequences used are
714 listed in Table S6.
715
716 **Construct design for split-GFP assays in *N. benthamiana* leaves and *Arabidopsis***
717 **transgenic plants**
718 The *UBQ10:sXVE:* S10-*At*CNIH5 clone was obtained as recently reported (Chiu et al.,

719 2024), and *UBQ10:sXVE:* S10-*At*CNIH5 1–26 and *UBQ10:sXVE:* S10-*At*CNIH5 1–132
720 were obtained through subcloning. For the transient expression of *At*PHT1;1-S11,
721 *At*SOS-S11, *At*DTX21-S11, *At*DTX35-S11, *At*URGT6-S11, *At*OCT1-S11, *At*HAK5-
722 S11, *At*VPE1-S11, and *At*SULTR1;3-S11, the CDS or the corresponding fragment was
723 amplified by PCR and subcloned into *UBQ10:sXVE*: (MCS)-S11 (Addgene plasmid #
724 108179). For subcellular localization analysis of the protein of interest, either
725 *UBQ10:sXVE:* S11-GFP1–9 (Addgene plasmid # 125665) or *UBQ10:sXVE:* GFP1–10
726 (Addgene plasmid # 125663) was co-expressed. For the tripartite split-GFP
727 reconstitution, the constructs encoding S10-tagged and S11-tagged protein fusions were
728 co-expressed in the presence of *UBQ10:sXVE*: GFP1–9 (Addgene plasmid # 108187).
729 Co-expression with 3xHA-S11 (Addgene plasmid # 108238) was used as a negative
730 control for protein–protein interaction. The brightness of the images for the protein–
731 protein interaction was adjusted by a 20% increase, and the contrast adjusted by a 20%
732 decrease. For the genomic GFP-*AtCNIH5* complemented plants (*AtCNIH5pro*: GFP-
733 *AtCNIH5/cnih5*), the construct design was recently described (Chiu et al., 2024). The
734 plasmid encoding *35S*: RFP-*At*CNIH5 was obtained as previously reported (Wudick *et*
735 *al.*, 2018). Primer sequences used are listed in Table S6.
736
737 ***Agrobacterium tumefaciens*-mediated infiltration of *N. benthamiana* leaves**
738 *Agrobacterium tumefaciens* strain EHA105 harboring the expression constructs or p19
739 was cultured in Luria–Bertani (LB) medium with the appropriate antibiotics [gentamicin
740 (50 μg ml^{-1}), rifampicin (5 μg ml^{-1}) or kanamycin (50 μg ml^{-1})]. Cells were resuspended
741 in the infiltration medium containing 10 mM $MgCl_2$, 10 mM MES (pH 7.5), and 150 μM
742 acetosyringone, and co-infiltrated to the true leaves of 3–5-week-old tobacco plants. For
743 the *β*-estradiol-inducible split-GFP system, 36.7 μM *β*-estradiol was applied as previously
744 described (Liu *et al.*, 2018; Liu, 2021). Infiltrated leaves were collected 2 days post-
745 infiltration (dpi) for confocal imaging.
746
747 **Confocal microscopy**
748 Confocal microscopy images were acquired using Zeiss LSM 800 (Zeiss) with objectives
749 Plan-Apochromat 10×/0.45 M27, 20×/0.8 M27, and 40×/1.3 Oil DIC M27 in multi-track
750 mode with line switching and averaging of two readings. Excitation/emission

751 wavelengths were 488 nm/410–546 nm for GFP, and 561 nm/656–617 nm for RFP, and
752 640 nm/656–700 nm for chlorophyll autofluorescence.
753
754 **Chemical treatments**
755 Acetosyringone (150 mM stock in DMSO; D134406; Sigma-Aldrich) was diluted to a
756 final concentration of 150 µM in ddH_2O. *β*-estradiol (36.7 mM stock in ethanol; E2758;
757 Sigma-Aldrich) was diluted to a final concentration of 36.7 µM in ddH_2O. For monitoring
758 the degradation of 1% Azo following the UV irradiation, 1% sodium 4-
759 hexylphenylazosulfonate (Na-Azo, Excenen Pharmatech) in 100 mM TEABC buffer was
760 1: 200 diluted and subjected to absorbance measurement.
761
762 **Accession Numbers**
763 Sequence data from this article can be found in the Arabidopsis Genome Initiative under
764 the following accession numbers: *At*CNIH5 (AT4G12090), *At*PHT1;1 (AT5G43350),
765 *At*PHT1;2 (AT5G43370), *At*PHT1;5 (AT2G32830), *At*PHT1;7 (AT3G54700), *At*PHT1;9
766 (AT1G76430), *At*LRK10L-1.1 (AT1G18390), *At*GXM2 (AT4G09990), *At*SOS
767 (AT1G26650), *At*DTX21 (AT1G33110), *At*DTX35 (AT4G25640), *At*URGT6
768 (AT1G34020), *At*OCT1 (AT1G73220), *At*HAK5 (AT4G13420), *At*VPE1 (AT3G47420),
769 *At*SULTR1;3 (AT1G22150).
770
771 **Supporting information**
772 **Fig. S1** Multiple marker abundance profiling (MMAP) of the identified proteins in Azo-
773 solubilized microsomal protein extraction (MME) samples. (A) Summary of label-free
774 proteomic analysis of microsomal proteins in *Arabidopsis* WT and *cnih5* Pi-limited roots.
775 (B) Relative number of high confidence marker (hcm) proteins for each compartment.
776 The relative number of distinct proteins for each compartment are displayed in the bar
777 graph as a percentage of all unique proteins in Arabidopsis (Standard) or all proteins in
778 the user sample (User). (C) Relative protein abundance of high hcm proteins for each
779 compartment. The Normalized Gator Abundance Factor (NGAF) scores for each protein
780 are summed *per* subcellular compartment according to the hcm assignments. The
781 abundance-scaling factor for each compartment describes the skew between the standard
782 observations in Arabidopsis (Standard) and the estimated abundance observation in the

783 user sample. The NGAF scores for each protein in the user sample is multiplied by the
784 compartmental scaling factor and summed per subcellular compartment according to the
785 hcm list. The sums for each compartment are displayed in the bar graph as a percentage
786 of the whole protein abundance (Standard) or all proteins in the total user sample (User).
787
788 **Fig. S2** Gene ontology (GO) analysis of the 4,317 identified proteins in iTRAQ-based
789 proteomics of *Arabidopsis* WT and *cnih5* Pi-limited roots. Dot plots of the top GO terms
790 in enrichment analysis for categories of molecular function (MF), biological process
791 (BP), and cellular component (CC) ranked by fold enrichment. Fold enrichment compares
792 the sample frequency representing the number of genes inputted under each GO term to
793 the background frequency of total genes annotated to the same term in *A. thaliana*. The
794 size of the dot represents the number of genes associated with each GO term. The more
795 intense reddish color reflects a lower adjusted *p*-value shown by $-\log_{10}$(FDR).
796
797 **Fig. S3** GO and KEGG pathway enrichment analyses of the 372 upregulated proteins and
798 the 51 upregulated integral microsomal proteins (MPs) in the Pi-limited root of *cnih5*. (A,
799 B) Dot plots of the gene ontology (GO) analyses of the 372 upregulated proteins (A) and
800 the 51 upregulated integral MPs (B) ranked by fold enrichment for categories of
801 molecular function, biological process, and cellular component. (C, D) Dot plots of the
802 KEGG pathway analyses of the 372 upregulated proteins (C) and the 51 upregulated
803 integral MPs (D) ranked by fold enrichment. Fold enrichment compares the sample
804 frequency representing the number of genes inputted under each GO term or KEGG term
805 to the background frequency of total genes annotated to the same term in *A. thaliana*. The
806 size of the dot indicates the number of genes in each GO term or KEGG term. The more
807 intense reddish color reflects a lower adjusted *p*-value, as indicated by $-\log_{10}$ (FDR).
808
809 **Fig. S4** GO and KEGG pathway enrichment analyses of the 106 downregulated proteins
810 in Pi-limited *cnih5* roots. (A, B) Dot plots of the GO (A) and KEGG pathway (B)
811 enrichment analyses ranked by fold enrichment. Fold enrichment compares the sample
812 frequency representing the number of genes inputted under each GO term or KEGG term
813 to the background frequency of total genes annotated to the same term in *A. thaliana*. The
814 size of the dot indicates the number of genes in each GO term or KEGG term. The more

815 intense reddish color reflects a lower adj. *p*-value adjusted *p*-value shown by
816 $-\log_{10}$(FDR).
817
818 **Fig. S5** Analysis of the interaction of PLVCub-*At*CNIH5 with NubG-*At*SOS, NubG-
819 *At*OCT1, NubG-*At*URGT6, NubG-*At*DTX21, and NubG-*At*DTX35 using the yeast split-
820 ubiquitin system (SUS). The co-expression of PLVCub-*At*CNIH5 with NubI and NubG
821 are used as positive and negative controls, respectively. Yeast transformants were grown
822 on synthetic medium without leucine and tryptophan (–LW; the left panel) or on synthetic
823 medium lacking leucine, tryptophan, and adenine with 500 μM methionine (–LWAH; the
824 middle panel) or on SC–LW containing 100 mg/L X-Gal (X-Gal; the right panel).
825
826 **Fig. S6** Amino acid sequence alignment of *Sc*Erv14 and *At*CNIHs. The sequence
827 alignment was performed using the Clustal Omega algorithm (Sievers et al., 2011) and
828 visualized using Jalview version 2.11.4.0 (Waterhouse et al., 2009). The degree of amino
829 acid conservation among the CNIHs is represented by a light-to-dark blue color gradient.
830 The transmembrane domains (TMD) are boxed by solid lines. The putative cornichon,
831 YLC, IFNLL, and acidic motifs are boxed by dotted lines. The protein sequences were
832 retrieved from UniprotKB (Uniprot ID: *Sc*Erv14, P53173; *At*CNIH1, Q9C7D7;
833 *At*CNIH2, Q3EDD7; *At*CNIH3, Q8GWT5; *At*CNIH4, Q84W04; *At*CNIH5, Q9SZ74).
834
835 **Fig. S7** Expression of *35S:* RFP-*At*CNIH5 in *Arabidopsis*. Expression of *35S*: RFP-
836 *At*CNIH5 in 5-day-old *Arabidopsis* seedlings grown under –P (0 μM KH_2PO_4, five days
837 of starvation) conditions. Scale bars, 50 μm.
838
839 **Fig. S8** Protein expression of the endogenous *At*CNIH5 in WT and GFP-*AtCNIH5* in the
840 *AtCNIH5pro*: GFP-*AtCNIH5/cnih5* complementation (COM) plants under Pi deficiency.
841 Immunoblot analysis of *At*CNIH5 and GFP-*AtCNIH5* in the root of *Arabidopsis* 11-day-
842 old WT and COM seedlings under –P (0 μM KH_2PO_4, seven days of starvation)
843 conditions. The bands of *At*CNIH5 and GFP-*AtCNIH5* are indicated by solid arrowhead
844 and open arrowhead, respectively.
845
846 **Table S1.** A list of the identified 4,317 proteins in *Arabidopsis* Pi-limited WT and *cnih5*

847 roots with GO enrichment analysis. Detailed descriptions of our proteomic analysis,
848 including the protein scores and mass, annotation, predicted transmembrane helices,
849 quantification for the identified proteins, and a list of the 57 overlapped identified proteins
850 between our datasets and the Pi starvation root proteome by Lan *et al.* (Lan et al., 2012).
851
852 **Table S2.** A list of the 372 upregulated and 106 downregulated proteins in Pi-limited
853 *cnih5* roots with GO enrichment analysis. Detailed descriptions, including annotation,
854 predicted transmembrane helices, and quantification for the proteins identified in
855 proteomic analysis.
856
857 **Table S3.** Downregulated proteins in Pi-limited *cnih5* roots compared to Pi-limited WT
858 roots by label-free proteomics across three biological replicates for each genotype.
859
860 **Table S4.** A list of the 19 root Pi starvation-induced (PSI) genes encoding transporters.
861 **Table S5.** Enrichment of root Pi starvation-induced (PSI) genes in the iTRAQ-based
862 proteomic analysis of Pi-limited *cnih5* roots.
863 **Table S6.** Oligonucleotides used for plasmid constructs.
864
865 **Acknowledgments**
866 This work was supported by the Ministry of Science and Technology (MOST 108-2311-
867 B-007-003-MY3) and the National Science and Technology Council (NSTC 112-2313-
868 B-007-001-MY3). We acknowledge Ms. He-Ting Yang for cloning the CDS of *At*OCT1,
869 *At*HAK5, *At*VPE1, and *At*SULTR1;3, and Mr. Po-Ruey Huang for cloning the constructs
870 expressing the truncated *At*CNIH5 variants. We also thank Mr. Cheng-Da Tsai for testing
871 the interaction of PLVCub-*At*CNIH5 with NubG-*At*PHT1;2, NubG-*At*PHT1;5, NubG-
872 *At*PHT1;7, and NubG-*At*PHT1;9. We thank Dr. Tzyy-Jen Chiou at Academia Sinica,
873 Taiwan (R.O.C.), for sharing anti-*At*PHO1 and anti-*At*PHF1 antibodies and the technical
874 support from the confocal imaging core (sponsored by MOST 110-2731-M-007-001),
875 National Tsing Hua University.
876
877 **Author Contributions**
878 T.-Y. L. conceived the project, designed the experiments, analyzed the experiments, and

879 wrote the article. M.-H. T., J.-Y. W., H.-F. L., C.-Y. C., H.-X. C. and C.-A. L. performed
880 and analyzed the experiments. T.-Y. L., M.-H. T. and J.-Y. W. contributed equally.
881
882 **Figure Legends**
883 **Fig. 1.** iTRAQ-based quantitative proteomic analysis of Pi-limited *Arabidopsis* roots. (A)
884 Schematic workflow of Azo-solubilized microsomal protein extraction for iTRAQ-based
885 quantitative proteomic analysis of *Arabidopsis* Pi-limited roots. (B) UV-Vis spectrum
886 monitoring the degradation of 1% Azo as a function of UV irradiation time.
887
888 **Fig. 2.** Immunoblot analysis of root microsomal proteins extracted from WT, *cnih5*, and
889 *pho2* mutants. (A, B) Protein expression of *At*NRT2.1, *At*PHT1;1/2/3, *At*PHT1;4,
890 *At*PHF1, and *At*PHO1 (A) and *At*CNIH5 (B) in the root of 11-day-old seedlings of
891 *Arabidopsis* WT, *cnih5*, and *pho2* under +P (250 μM KH_2PO_4) and –P (0 μM KH_2PO_4,
892 five days of starvation) conditions. The band of *At*CNIH5 is indicated by arrowhead. The
893 relative protein expression level was normalized with the corresponding amido black
894 staining and relative to the WT control. Error bars represent SE (n = 2–3). The applied
895 extraction methods were shown as indicated. MME, microsomal protein extraction.
896
897 **Fig. 3**. Summary of iTRAQ-based proteomic analysis of microsomal proteins (MPs) in
898 Pi-limited WT and *cnih5* roots. (A) Venn diagram for comparing MPs and
899 transmembrane (TM) proteins of the 4,317 identified proteins. Subcellular localization
900 was analyzed by SUBA5. TM protein prediction or annotation was performed by
901 deepTMHMM or UniprotKB. (B) Distribution of subcellular localizations of the
902 identified 4,317 proteins analyzed by SUBA5. Note that not all proteins are restricted to
903 a single subcellular location. (C) Distribution of subcellular localizations of the 915
904 integral MPs among the identified 1,231 TM proteins analyzed by SUBA5. Note that not
905 all proteins are restricted to a single subcellular location. (D) Volcano plots of
906 differentially expressed proteins (DEPs) in the Pi-limited root of *cnih5*. Results of the
907 four comparison groups (four ratios of *cnih5* versus WT) were shown separately, with the
908 $-\log_{10}$FDR adj. *p*-value plotted against the $\log_2$ fold-change (FC). The vertical dash lines
909 denote ±1.25-FC (Log_2 FC ≈ 0.322 and Log_2FC ≈ −0.415), while the horizontal dash line
910 denotes FDR adj. *p*-value = 0.05. Upregulated and downregulated proteins are indicated

911 by red and blue dots, respectively. Only DEPs with ±2-FC are marked in red or blue. The
912 *At*PHT1s and *At*PHF1 are marked in green.
913
914 **Fig 4.** Interactive graph of enriched GO terms and semantic similarities for the 106
915 downregulated proteins in the Pi-limited *cnih5* roots. Enriched GO terms of (A) molecular
916 function, (B) biological process, and (C) cellular component identified by ShinyGO were
917 summarized using REVIGO to remove redundancy and cluster functionally related terms
918 in *A. thaliana*. Each node represents a GO term, with color intensity reflecting Log_{10}
919 (enrichment factor). The node size is proportional to the Log_{10} value of the number of
920 gene annotations for each term in the background database. Lines between nodes
921 represent semantic similarity, and line thickness indicates the degree of functional overlap
922 between terms.
923
924 **Fig. 5**. Analysis of the interaction of *At*CNIH5 with its potential ER cargoes by the yeast
925 split-ubiquitin system. (A, B) Co-expression of PLVCub-*At*CNIH5 with NubG-
926 *At*PHT1;2, NubG-*At*PHT1;5, NubG-*At*PHT1;7, and NubG-*At*PHT1;9 (A) or *At*LRK10L-
927 1.1-NubG, *At*SOS-NubG, *At*OCT1-NubG, *At*URGT6-NubG, NubG-*At*GXM2,
928 *At*DTX21-NubG, and *At*DTX35- NubG (B). The co-expression of PLVCub-*At*CNIH5
929 with NubI and NubG are used as positive and negative controls, respectively. Yeast
930 transformants were grown on synthetic medium without leucine and tryptophan (–LW;
931 the left panel) or on synthetic medium lacking leucine, tryptophan, adenine, and histidine
932 with 500 μM methionine (–LWAH; middle panel) or on SC–LW containing 100 mg/L
933 X-Gal (X-Gal; the right panel).
934
935 **Fig. 6.** Analysis of the interaction of *At*CNIH5 with its potential ER cargoes by the
936 tripartite split-GFP assay in *N. benthamiana* leaves. (A, B) Expression and subcellular
937 localization (A) and protein–protein interaction analysis (B) of S10-*At*CNIH5 with
938 *At*PHT1;1-S11, 3xHA-S11, *At*SOS-S11, *At*OCT1-S11, *At*HAK5-S11, *At*SULTR1;3-S11,
939 *At*URGT6-S11, *At*DTX21-S11, *At*DTX35-S11, or *At*VPE1-S11. The co-expression of
940 S10-*At*CNIH5 with *At*PHT1;1-S11 and 3xHA-S11 are used as positive and negative
941 controls, respectively. The percentage of laser power used for acquisition is shown. Scale
942 bars, 5 μm. Red signals show autofluorescence from chloroplasts.

943

944 **Fig. 7.** Analysis of the interaction of *At*PHT1;1 with the truncated *At*CNIH5 variants. (A)
945 Schematic diagram of full-length (FL) and truncated *At*CNIH5 variants. The lengths of
946 the truncated variants are indicated by the number of residues. The transmembrane
947 domains and the putative cornichon, YLC, IFNLL, and acidic motifs are shown. The
948 black box, the transmembrane domain (TMD); the blue box, the cornichon motif; the
949 green box, the YLC motif; the yellow box, the IFNLL motif. The red box, the acidic
950 motif. The gray box shows the sequence alignment of the putative acidic motif of *Sc*Erv14
951 and *At*CNIHs. Noted that *At*CNIH5 has a shorter C-terminal tail carrying only one acidic
952 residue D134. (B) Co-expression of *At*PHT1;1-PLVCub with NubG-*At*CNIH5, NubG-
953 *At*CNIH5 1–26, NubG-*At*CNIH5 1–49, NubG-*At*CNIH5 1–92, and NubG-*At*CNIH5 1–
954 132 in yeast split ubiquitin assay. The co-expression of *At*PHT1;1-PLVCub with NubI
955 and NubG are used as positive and negative controls, respectively. Yeast transformants
956 were grown on synthetic medium without leucine and tryptophan (–LW; the left panel)
957 or on synthetic medium lacking leucine, tryptophan, adenine, and histidine with 500 μM
958 methionine (–LWAH; middle panel) or on SC–LW containing 100 mg/L X-Gal (X-Gal;
959 the right panel). (C) Expression and subcellular localization of S10-*At*CNIH5 1–26 and
960 S10-*At*CNIH5 1–132 in *N. benthamiana* leaves. Scale bars, 5 μm .(D) Protein–protein
961 interaction analysis of *At*PHT1;1-S11, *At*DTX21-S11, or *At*OCT1-S11 with S10-
962 *At*CNIH5 1–26 or S10-*At*CNIH5 1–132 in *N. benthamiana* leaves. The percentage of
963 laser power used for acquisition is shown. Scale bars, 5 μm.
964

965 **Fig. 8.** Increasing *in-situ At*CNIH5 expression/activity boosts plant growth.
966 The shoot and root fresh weight (FW) of *Arabidopsis* 11-day-old WT, *cnih5* and
967 *AtCNIH5pro*: GFP-*AtCNIH5/cnih5* complementation (COM) lines under +P (250 μM
968 KH_2PO_4), modest –P (0 μM KH_2PO_4, three days of starvation or 50 μM KH_2PO_4, eleven
969 days of starvation), and severe –P (0 μM KH_2PO_4, eleven days of starvation) conditions.
970 Data are visualized using BoxPlotR (Spitzer *et al*., 2014). Center lines show the medians;
971 the central plus signs (+) show the means; box limits indicate the 25th and 75th
972 percentiles; whiskers extend to the 5th and 95th percentiles, and data points are plotted
973 as dots. Data significantly different from the other groups are indicated by different
974 lowercase letters (n, pools of seedings from independent experiments; One-Way

975 ANOVA, Duncan's test).

976

977 **Fig. 9**. *At*CNIH5-mediated ER-to-Golgi transport of membrane proteins associated with
978 Pi starvation responses in *Arabidopsis* root.
979 Under Pi starvation (−P), the transcripts of *CNIH5*, *PHT1* genes, *OCT1*, *GXM2*, and
980 *DTX35* increase in *Arabidopsis* root cells (Liu *et al.*, 2016). As an ER cargo receptor,
981 CNIH5 assists the ER export of the newly synthesized PHT1s, LRK10L-1.1, SOS, OCT1,
982 URGT6, GXM2, DTX21, and DTX35, and their loading into COPII vesicles, thereby
983 directing them to their corresponding subcellular destinations.

984

985 **Table 1.** Summary of *At*PHT1s and *At*PHF1 abundance in Pi-limited WT and *cnih5* roots.
986 The normalized ratios compared the protein expression in Col-0_1, Col-0_2, *cnih5*_1,
987 and *cnih5*_2 samples. The FDR adj. *p*-values are in parentheses.

988

989 **Table 2.** List of the 31 downregulated microsomal transmembrane proteins in Pi-limited
990 *cnih5* roots.
991 The normalized ratios compared the protein expression in Col-0_1, Col-0_2, *cnih5*_1,
992 and *cnih5*_2 samples. The FDR adj. *p*-values are in parentheses. The candidates
993 highlighted in gray are selected for testing protein–protein interaction in this study.
994 Subcellular localization is predicted or annotated by SUBA5, UniprotKB or experimental
995 data.

996

997 **References**

998 **Abas L, Luschnig C** (2010) Maximum yields of microsomal-type membranes from small
999 amounts of plant material without requiring ultracentrifugation. Analytical
1000 Biochemistry **401:** 217-227
1001 **Arpat AB, Magliano P, Wege S, Rouached H, Stefanovic A, Poirier Y** (2012)
1002 Functional expression of PHO1 to the Golgi and *trans*-Golgi network and its role
1003 in export of inorganic phosphate. The Plant Journal **71:** 479-491
1004 **Barlowe CK, Miller EA** (2013) Secretory Protein Biogenesis and Traffic in the Early
1005 Secretory Pathway. Genetics **193:** 383-410
1006 **Bayle V, Arrighi J-F, Creff A, Nespoulous C, Vialaret J, Rossignol M, Gonzalez E,**
1007 **Paz-Ares J, Nussaume L** (2011) *Arabidopsis thaliana* High-Affinity Phosphate
1008 Transporters Exhibit Multiple Levels of Posttranslational Regulation. The Plant
1009 Cell **23:** 1523-1535
1010 **Bökel C, Dass S, Wilsch-Bräuninger M, Roth S** (2006) *Drosophila* Cornichon acts as
1011 cargo receptor for ER export of the TGFα-like growth factor Gurken.

1012 Development **133:** 459-470
1013 **Bowtell D, Fu P, Simon M, Senior P** (1992) Identification of murine homologues of the
1014 Drosophila son of sevenless gene: potential activators of ras. Proceedings of the
1015 National Academy of Sciences **89:** 6511-6515
1016 **Brown KA, Chen B, Guardado-Alvarez TM, Lin Z, Hwang L, Ayaz-Guner S, Jin S,**
1017 **Ge Y** (2019) A photocleavable surfactant for top-down proteomics. Nature
1018 Methods **16:** 417-420
1019 **Brown KA, Tucholski T, Eken C, Knott S, Zhu Y, Jin S, Ge Y** (2020) High-
1020 Throughput Proteomics Enabled by a Photocleavable Surfactant. Angewandte
1021 Chemie International Edition **59:** 8406-8410
1022 **Chen J, Wang Y, Wang F, Yang J, Gao M, Li C, Liu Y, Liu Y, Yamaji N, Ma JF,**
1023 **Paz-Ares J, Nussaume L, Zhang S, Yi K, Wu Z, Wu P** (2015) The Rice CK2
1024 Kinase Regulates Trafficking of Phosphate Transporters in Response to
1025 Phosphate Levels. The Plant Cell **27:** 711-723
1026 **Chiu C-Y, Tsai C-D, Wang J-Y, Tsai M-H, Kanno S, Lung H-F, Liu T-Y** (2024)
1027 Phosphate Starvation-Induced CORNICHON HOMOLOG 5 as Endoplasmic
1028 Reticulum Cargo Receptor for PHT1 Transporters in *Arabidopsis*. bioRxiv**:**
1029 2024.2006.2020.599911
1030 **Chopin F, Wirth J, Dorbe M-F, Lejay L, Krapp A, Gojon A, Daniel-Vedele F** (2007)
1031 The Arabidopsis nitrate transporter AtNRT2.1 is targeted to the root plasma
1032 membrane. Plant Physiology and Biochemistry **45:** 630-635
1033 **Dancourt J, Barlowe C** (2010) Protein Sorting Receptors in the Early Secretory
1034 Pathway. Annual Review of Biochemistry **79:** 777-802
1035 **de Torres-Zabala M, Truman W, Bennett MH, Lafforgue G, Mansfield JW,**
1036 **Rodriguez Egea P, Bögre L, Grant M** (2007) *Pseudomonas syringae* pv. *tomato*
1037 hijacks the *Arabidopsis* abscisic acid signalling pathway to cause disease. The
1038 EMBO Journal **26:** 1434-1443
1039 **Deutsch EW, Bandeira N, Perez-Riverol Y, Sharma V, Carver Jeremy J, Mendoza**
1040 **L, Kundu DJ, Wang S, Bandla C, Kamatchinathan S, Hewapathirana S,**
1041 **Pullman Benjamin S, Wertz J, Sun Z, Kawano S, Okuda S, Watanabe Y,**
1042 **MacLean B, MacCoss Michael J, Zhu Y, Ishihama Y, Vizcaíno Juan A** (2022)
1043 The ProteomeXchange consortium at 10 years: 2023 update. Nucleic Acids
1044 Research **51:** D1539-D1548
1045 **Evenson KJ, Post-Beittenmiller D** (1995) Fatty Acid-Elongating Activity in Rapidly
1046 Expanding Leek Epidermis. Plant Physiology **109:** 707-716
1047 **Ge SX, Jung D, Yao R** (2019) ShinyGO: a graphical gene-set enrichment tool for
1048 animals and plants. Bioinformatics **36:** 2628-2629
1049 **González E, Solano R, Rubio V, Leyva A, Paz-Ares J** (2005) PHOSPHATE
1050 TRANSPORTER TRAFFIC FACILITATOR1 Is a Plant-Specific SEC12-
1051 Related Protein That Enables the Endoplasmic Reticulum Exit of a High-Affinity
1052 Phosphate Transporter in *Arabidopsis*. The Plant Cell **17:** 3500-3512
1053 **Hallgren J, Tsirigos KD, Pedersen MD, Almagro Armenteros JJ, Marcatili P,**
1054 **Nielsen H, Krogh A, Winther O** (2022) DeepTMHMM predicts alpha and beta
1055 transmembrane proteins using deep neural networks. bioRxiv**:**
1056 2022.2004.2008.487609
1057 **Harmel N, Cokic B, Zolles G, Berkefeld H, Mauric V, Fakler B, Stein V, Klöcker N**
1058 (2012) AMPA Receptors Commandeer an Ancient Cargo Exporter for Use as an
1059 Auxiliary Subunit for Signaling. PLOS ONE **7:** e30681

1060 **Hiroguchi A, Sakamoto S, Mitsuda N, Miwa K** (2021) Golgi-localized membrane
1061 protein AtTMN1/EMP12 functions in the deposition of rhamnogalacturonan II
1062 and I for cell growth in Arabidopsis. Journal of Experimental Botany **72:** 3611-
1063 3629
1064 **Hooper CM, Castleden IR, Tanz SK, Aryamanesh N, Millar AH** (2016) SUBA4: the
1065 interactive data analysis centre for Arabidopsis subcellular protein locations.
1066 Nucleic Acids Research **45:** D1064-D1074
1067 **Huang T-K, Han C-L, Lin S-I, Chen Y-J, Tsai Y-C, Chen Y-R, Chen J-W, Lin W-**
1068 **Y, Chen P-M, Liu T-Y, Chen Y-S, Sun C-M, Chiou T-J** (2013) Identification
1069 of Downstream Components of Ubiquitin-Conjugating Enzyme PHOSPHATE2
1070 by Quantitative Membrane Proteomics in *Arabidopsis* Roots. The Plant Cell **25:**
1071 4044-4060
1072 **Krogh A, Larsson B, von Heijne G, Sonnhammer ELL** (2001) Predicting
1073 transmembrane protein topology with a hidden markov model: application to
1074 complete genomes. Journal of Molecular Biology **305:** 567-580
1075 **Kurokawa K, Nakano A** (2018) The ER exit sites are specialized ER zones for the
1076 transport of cargo proteins from the ER to the Golgi apparatus. The Journal of
1077 Biochemistry **165:** 109-114
1078 **Lagunas-Gomez D, Yañez-Dominguez C, Zavala-Padilla G, Barlowe C, Pantoja O**
1079 (2023) The C-terminus of the cargo receptor Erv14 affects COPII vesicle
1080 formation and cargo delivery. Journal of Cell Science **136**
1081 **Lan P, Li W, Schmidt W** (2012) Complementary Proteome and Transcriptome Profiling
1082 in Phosphate-deficient Arabidopsis Roots Reveals Multiple Levels of Gene
1083 Regulation. Molecular & Cellular Proteomics **11:** 1156-1166
1084 **Lee C, Teng Q, Zhong R, Yuan Y, Haghighat M, Ye Z-H** (2012) Three Arabidopsis
1085 DUF579 Domain-Containing GXM Proteins are Methyltransferases Catalyzing
1086 4-*O*-Methylation of Glucuronic Acid on Xylan. Plant and Cell Physiology **53:**
1087 1934-1949
1088 **Lee S-B, Jung S-J, Go Y-S, Kim H-U, Kim J-K, Cho H-J, Park OK, Suh M-C** (2009)
1089 Two Arabidopsis 3-ketoacyl CoA synthase genes, *KCS20* and *KCS2/DAISY*, are
1090 functionally redundant in cuticular wax and root suberin biosynthesis, but
1091 differentially controlled by osmotic stress. The Plant Journal **60:** 462-475
1092 **Lelandais-Brière C, Jovanovic M, Torres GAM, Perrin Y, Lemoine R, Corre-**
1093 **Menguy F, Hartmann C** (2007) Disruption of *AtOCT1*, an organic cation
1094 transporter gene, affects root development and carnitine-related responses in
1095 Arabidopsis. The Plant Journal **51:** 154-164
1096 **Liao Y-Y, Buckhout TJ, Schmidt W** (2011) Phosphate deficiency-induced cell wall
1097 remodeling. Plant Signaling & Behavior **6:** 700-702
1098 **Lim CW, Yang SH, Shin KH, Lee SC, Kim SH** (2015) The AtLRK10L1.2, *Arabidopsis*
1099 ortholog of wheat LRK10, is involved in ABA-mediated signaling and drought
1100 resistance. Plant Cell Reports **34:** 447-455
1101 **Lin W-D, Liao Y-Y, Yang TJW, Pan C-Y, Buckhout TJ, Schmidt W** (2011)
1102 Coexpression-Based Clustering of Arabidopsis Root Genes Predicts Functional
1103 Modules in Early Phosphate Deficiency Signaling. Plant Physiology **155:** 1383-
1104 1402
1105 **Lin W-Y, Huang T-K, Chiou T-J** (2013) NITROGEN LIMITATION ADAPTATION,
1106 a Target of MicroRNA827, Mediates Degradation of Plasma Membrane–
1107 Localized Phosphate Transporters to Maintain Phosphate Homeostasis in

Arabidopsis. The Plant Cell **25:** 4061-4074

Liu T-Y (2021) Using Tripartite Split-sfGFP for the Study of Membrane Protein–Protein Interactions. *In* JJ Sanchez-Serrano, J Salinas, eds, Arabidopsis Protocols. Springer US, New York, NY, pp 323-336

Liu T-Y, Chou W-C, Chen W-Y, Chu C-Y, Dai C-Y, Wu P-Y (2018) Detection of membrane protein–protein interaction *in planta* based on dual-intein-coupled tripartite split-GFP association. The Plant Journal **94:** 426-438

Liu T-Y, Huang T-K, Tseng C-Y, Lai Y-S, Lin S-I, Lin W-Y, Chen J-W, Chiou T-J (2012) PHO2-Dependent Degradation of PHO1 Modulates Phosphate Homeostasis in *Arabidopsis*. The Plant Cell **24:** 2168-2183

Liu T-Y, Huang T-K, Yang S-Y, Hong Y-T, Huang S-M, Wang F-N, Chiang S-F, Tsai S-Y, Lu W-C, Chiou T-J (2016) Identification of plant vacuolar transporters mediating phosphate storage. Nature Communications **7:** 11095

Mølhøj M, Verma R, Reiter W-D (2004) The Biosynthesis of d-Galacturonate in Plants. Functional Cloning and Characterization of a Membrane-Anchored UDP-d-Glucuronate 4-Epimerase from Arabidopsis. Plant Physiology **135:** 1221-1230

Mouille G, Ralet M-C, Cavelier C, Eland C, Effroy D, Hématy K, McCartney L, Truong HN, Gaudon V, Thibault J-F, Marchant A, Höfte H (2007) Homogalacturonan synthesis in *Arabidopsis thaliana* requires a Golgi-localized protein with a putative methyltransferase domain. The Plant Journal **50:** 605-614

Nakanishi H, Suda Y, Neiman AM (2007) Erv14 family cargo receptors are necessary for ER exit during sporulation in *Saccharomyces cerevisiae*. Journal of Cell Science **120:** 908-916

Nguyen TV, Gupta R, Annas D, Yoon J, Kim Y-J, Lee GH, Jang JW, Park KH, Rakwal R, Jung K-H, Min CW, Kim ST (2021) An Integrated Approach for the Efficient Extraction and Solubilization of Rice Microsomal Membrane Proteins for High-Throughput Proteomics. Frontiers in Plant Science **12**

Nussaume L, Kanno S, Javot H, Marin E, Nakanishi TM, Thibaud M-C (2011) Phosphate Import in Plants: Focus on the PHT1 Transporters. Frontiers in Plant Science **2**

Obrdlik P, El-Bakkoury M, Hamacher T, Cappellaro C, Vilarino C, Fleischer C, Ellerbrok H, Kamuzinzi R, Ledent V, Blaudez D, Sanders D, Revuelta JL, Boles E, André B, Frommer WB (2004) K^+ channel interactions detected by a genetic system optimized for systematic studies of membrane protein interactions. Proceedings of the National Academy of Sciences **101:** 12242-12247

Pagant S, Wu A, Edwards S, Diehl F, Miller Elizabeth A (2015) Sec24 Is a Coincidence Detector that Simultaneously Binds Two Signals to Drive ER Export. Current Biology **25:** 403-412

Park BS, Seo JS, Chua N-H (2014) NITROGEN LIMITATION ADAPTATION Recruits PHOSPHATE2 to Target the Phosphate Transporter PT2 for Degradation during the Regulation of *Arabidopsis* Phosphate Homeostasis. The Plant Cell **26:** 454-464

Perez-Riverol Y, Bandla C, Kundu Deepti J, Kamatchinathan S, Bai J, Hewapathirana S, John Nithu S, Prakash A, Walzer M, Wang S, Vizcaíno Juan A (2024) The PRIDE database at 20 years: 2025 update. Nucleic Acids Research **53:** D543-D553

Poirier Y, Bucher M (2002) Phosphate Transport and Homeostasis in Arabidopsis. The Arabidopsis Book **2002**

1156 **Poirier Y, Jaskolowski A, Clúa J** (2022) Phosphate acquisition and metabolism in
1157 plants. Current Biology **32:** R623-R629
1158 **Powers J, Barlowe C** (1998) Transport of Axl2p Depends on Erv14p, an ER–Vesicle
1159 Protein Related to the *Drosophila cornichon* Gene Product. Journal of Cell
1160 Biology **142:** 1209-1222
1161 **Powers J, Barlowe C** (2002) Erv14p Directs a Transmembrane Secretory Protein into
1162 COPII-coated Transport Vesicles. Molecular Biology of the Cell **13:** 880-891
1163 **R Core Team** (2021) R: A Language and Environment for Statistical Computing. R
1164 Foundation for Statistical Computing
1165 **Ramel F, Sulmon C, Cabello-Hurtado F, Taconnat L, Martin-Magniette M-L,**
1166 **Renou J-P, El Amrani A, Couée I, Gouesbet G** (2007) Genome-wide
1167 interacting effects of sucrose and herbicide-mediated stress in *Arabidopsis*
1168 *thaliana*: novel insights into atrazine toxicity and sucrose-induced tolerance.
1169 BMC Genomics **8:** 450
1170 **Rosas-Santiago P, Lagunas-Gómez D, Barkla BJ, Vera-Estrella R, Lalonde S, Jones**
1171 **A, Frommer WB, Zimmermannova O, Sychrová H, Pantoja O** (2015)
1172 Identification of rice cornichon as a possible cargo receptor for the Golgi-
1173 localized sodium transporter OsHKT1;3. Journal of Experimental Botany **66:**
1174 2733-2748
1175 **Rosas-Santiago P, Lagunas-Gomez D, Yáñez-Domínguez C, Vera-Estrella R,**
1176 **Zimmermannová O, Sychrová H, Pantoja O** (2017) Plant and yeast cornichon
1177 possess a conserved acidic motif required for correct targeting of plasma
1178 membrane cargos. Biochimica et Biophysica Acta (BBA) - Molecular Cell
1179 Research **1864:** 1809-1818
1180 **Roth S, Shira Neuman-Silberberg F, Barcelo G, Schüpbach T** (1995) cornichon and
1181 the EGF receptor signaling process are necessary for both anterior-posterior and
1182 dorsal-ventral pattern formation in Drosophila. Cell **81:** 967-978
1183 **RStudio Team** (2020) RStudio: Integrated Development Environment for R. RStudio,
1184 PBC
1185 **Saez-Aguayo S, Parra-Rojas JP, Sepúlveda-Orellana P, Celiz-Balboa J, Arenas-**
1186 **Morales V, Sallé C, Salinas-Grenet H, Largo-Gosens A, North HM, Ralet M-**
1187 **C, Orellana A** (2020) Transport of UDP-rhamnose by URGT2, URGT4, and
1188 URGT6 modulates rhamnogalacturonan-I length. Plant Physiology **185:** 914-933
1189 **Salazar-Henao JE, Schmidt W** (2016) An Inventory of Nutrient-Responsive Genes in
1190 *Arabidopsis* Root Hairs. Frontiers in Plant Science **7**
1191 **Sievers F, Wilm A, Dineen D, Gibson TJ, Karplus K, Li W, Lopez R, McWilliam H,**
1192 **Remmert M, Söding J, Thompson JD, Higgins DG** (2011) Fast, scalable
1193 generation of high-quality protein multiple sequence alignments using Clustal
1194 Omega. Molecular Systems Biology **7:** 539
1195 **Slowikowski K, Schep A, Hughes S, Kien Dang T, Lukauskas S, Irisson J-O,**
1196 **Kamvar ZN, Ryan T, Christophe D, Hiroaki Y, Gramme P, Abdol AM,**
1197 **Barrett M, Cannoodt R, Krassowski M, Chirico M, Aphalo P, Barton F**
1198 (2024) ggrepel: Automatically Position Non-Overlapping Text Labels with
1199 'ggplot2'. *In*,
1200 **Spitzer M, Wildenhain J, Rappsilber J, Tyers M** (2014) BoxPlotR: a web tool for
1201 generation of box plots. Nature Methods **11:** 121-122
1202 **Sterling JD, Atmodjo MA, Inwood SE, Kumar Kolli VS, Quigley HF, Hahn MG,**
1203 **Mohnen D** (2006) Functional identification of an *Arabidopsis* pectin biosynthetic

1204 homogalacturonan galacturonosyltransferase. Proceedings of the National
1205 Academy of Sciences **103:** 5236-5241
1206 **The UniProt Consortium** (2023) UniProt: the Universal Protein Knowledgebase in
1207 2023. Nucleic Acids Research **51:** D523-D531
1208 **Tian T, Liu Y, Yan H, You Q, Yi X, Du Z, Xu W, Su Z** (2017) agriGO v2.0: a GO
1209 analysis toolkit for the agricultural community, 2017 update. Nucleic Acids
1210 Research **45:** W122-W129
1211 **Urbanowicz BR, Peña MJ, Ratnaparkhe S, Avci U, Backe J, Steet HF, Foston M, Li**
1212 **H, O'Neill MA, Ragauskas AJ, Darvill AG, Wyman C, Gilbert HJ, York WS**
1213 (2012) 4-*O*-methylation of glucuronic acid in *Arabidopsis* glucuronoxylan is
1214 catalyzed by a domain of unknown function family 579 protein. Proceedings of
1215 the National Academy of Sciences **109:** 14253-14258
1216 **Wang X, Liang S** (2012) Sample preparation for the analysis of membrane proteomes
1217 by mass spectrometry. Protein & Cell **3:** 661-668
1218 **Waterhouse AM, Procter JB, Martin DMA, Clamp M, Barton GJ** (2009) Jalview
1219 Version 2—a multiple sequence alignment editor and analysis workbench.
1220 Bioinformatics **25:** 1189-1191
1221 **Wei L, Liu L, Chen Z, Huang Y, Yang L, Wang P, Xue S, Bie Z** (2023) CmCNIH1
1222 improves salt tolerance by influencing the trafficking of CmHKT1;1 in pumpkin.
1223 The Plant Journal **114:** 1353-1368
1224 **Wickham H** (2023) stringr: Simple, Consistent Wrappers for Common String
1225 Operations. *In*,
1226 **Wickham H, Chang W, Henry L, Lin Pedersen T, Takahashi K, Wilke C, Woo K,**
1227 **Yutani H, Dunnington D, van den Brand T** (2016) ggplot2: Elegant Graphics
1228 for Data Analysis. *In*. Springer-Verlag New York
1229 **Wu X, Lai Y, Rao S, Lv L, Ji M, Han K, Weng J, Lu Y, Peng J, Lin L, Wu G, Chen**
1230 **J, Yan F, Zheng H** (2021) Genome-Wide Identification Reveals That *Nicotiana*
1231 *benthamiana* Hypersensitive Response (HR)-Like Lesion Inducing Protein 4
1232 (NbHRLI4) Mediates Cell Death and Salicylic Acid-Dependent Defense
1233 Responses to Turnip Mosaic Virus. Frontiers in Plant Science **12**
1234 **Wudick MM, Portes MT, Michard E, Rosas-Santiago P, Lizzio MA, Nunes CO,**
1235 **Campos C, Santa Cruz Damineli D, Carvalho JC, Lima PT, Pantoja O, Feijó**
1236 **JA** (2018) CORNICHON sorting and regulation of GLR channels underlie pollen
1237 tube Ca^{2+} homeostasis. Science **360:** 533-536
1238 **Yáñez-Domínguez C, Lagunas-Gómez D, Torres-Cifuentes DM, Bezanilla M,**
1239 **Pantoja O** (2023) A cornichon protein controls polar localization of the PINA
1240 auxin transporter in *Physcomitrium patens*. Development **150**
1241 **Yang Z, Yang J, Wang Y, Wang F, Mao W, He Q, Xu J, Wu Z, Mao C** (2020)
1242 PROTEIN PHOSPHATASE95 Regulates Phosphate Homeostasis by Affecting
1243 Phosphate Transporter Trafficking in Rice. The Plant Cell **32:** 740-757
1244 **Yoshimoto K, Hanaoka H, Sato S, Kato T, Tabata S, Noda T, Ohsumi Y** (2004)
1245 Processing of ATG8s, Ubiquitin-Like Proteins, and Their Deconjugation by
1246 ATG4s Are Essential for Plant Autophagy. The Plant Cell **16:** 2967-2983
1247 **Yuan Y, Teng Q, Lee C, Zhong R, Ye Z-H** (2014) Modification of the degree of 4-*O*-
1248 methylation of secondary wall glucuronoxylan. Plant Science **219-220:** 42-50
1249 **Zhang H, Guo Z, Zhuang Y, Suo Y, Du J, Gao Z, Pan J, Li L, Wang T, Xiao L, Qin**
1250 **G, Jiao Y, Cai H, Li L** (2021) MicroRNA775 regulates intrinsic leaf size and
1251 reduces cell wall pectin levels by targeting a galactosyltransferase gene in

1252 Arabidopsis. The Plant Cell **33:** 581-602
1253 **Zhang H, Zhao F-G, Tang R-J, Yu Y, Song J, Wang Y, Li L, Luan S** (2017) Two
1254 tonoplast MATE proteins function as turgor-regulating chloride channels in
1255 *Arabidopsis*. Proceedings of the National Academy of Sciences **114:** E2036-
1256 E2045
1257 **Zheng J, Yao L, Zeng X, Wang B, Pan L** (2023) *ERV14* receptor impacts mycelial
1258 growth via its interactions with cell wall synthase and transporters in *Aspergillus*
1259 *niger*. Frontiers in Microbiology **14**
1260 **Zhou M, Zhu S, Mo X, Guo Q, Li Y, Tian J, Liang C** (2022) Proteomic Analysis
1261 Dissects Molecular Mechanisms Underlying Plant Responses to Phosphorus
1262 Deficiency. Cells **11:** 651
1263 **Zimmermannová O, Felcmanová K, Rosas-Santiago P, Papoušková K, Pantoja O,**
1264 **Sychrová H** (2019) Erv14 cargo receptor participates in regulation of plasma-
1265 membrane potential, intracellular pH and potassium homeostasis via its
1266 interaction with K^+-specific transporters Trk1 and Tok1. Biochimica et
1267 Biophysica Acta (BBA) - Molecular Cell Research **1866:** 1376-1388
1268

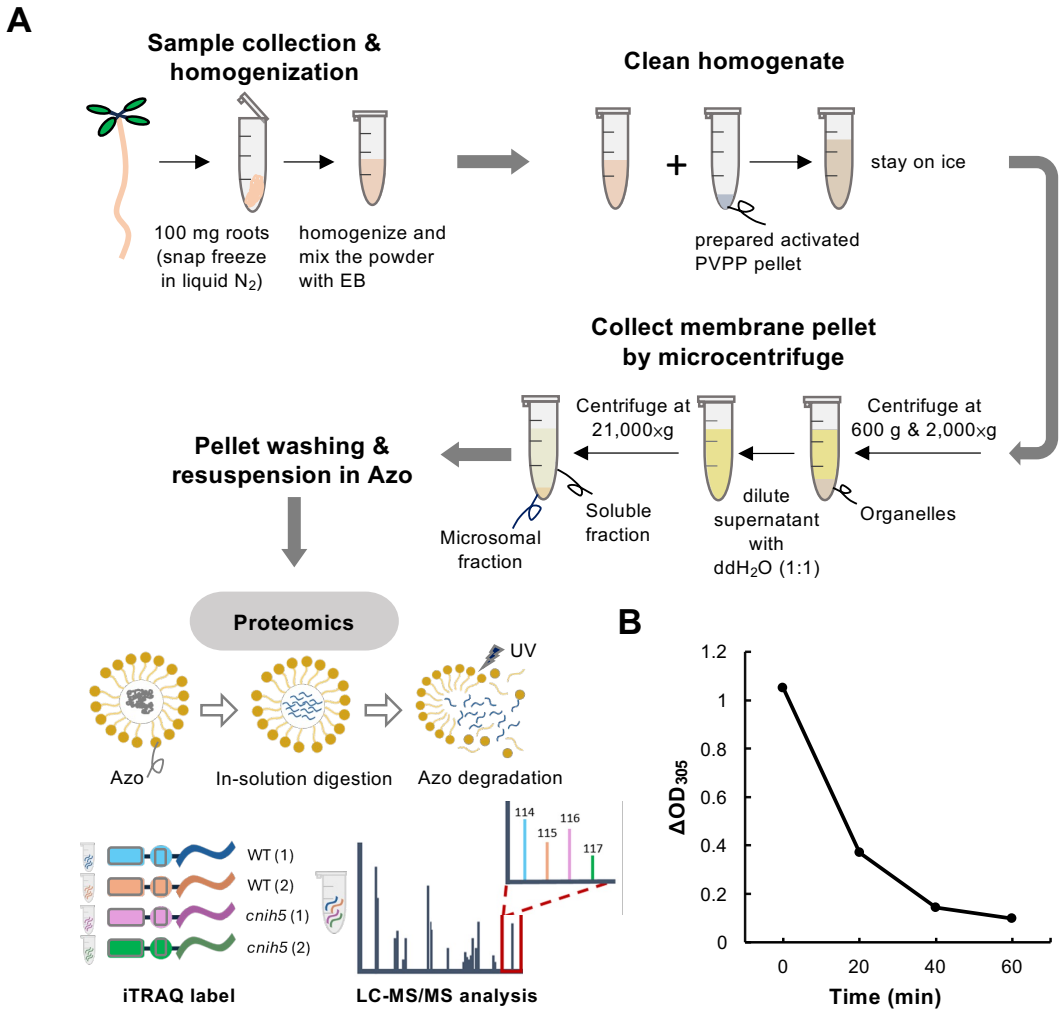

Fig 1. iTRAQ-based quantitative proteomic analysis of Pi-limited *Arabidopsis* roots. (A) Schematic workflow of Azo-solubilized microsomal protein extraction for iTRAQ-based quantitative proteomic analysis of *Arabidopsis* Pi-limited roots. (B) UV-Vis spectrum monitoring the degradation of 1% Azo as a function of UV irradiation time.

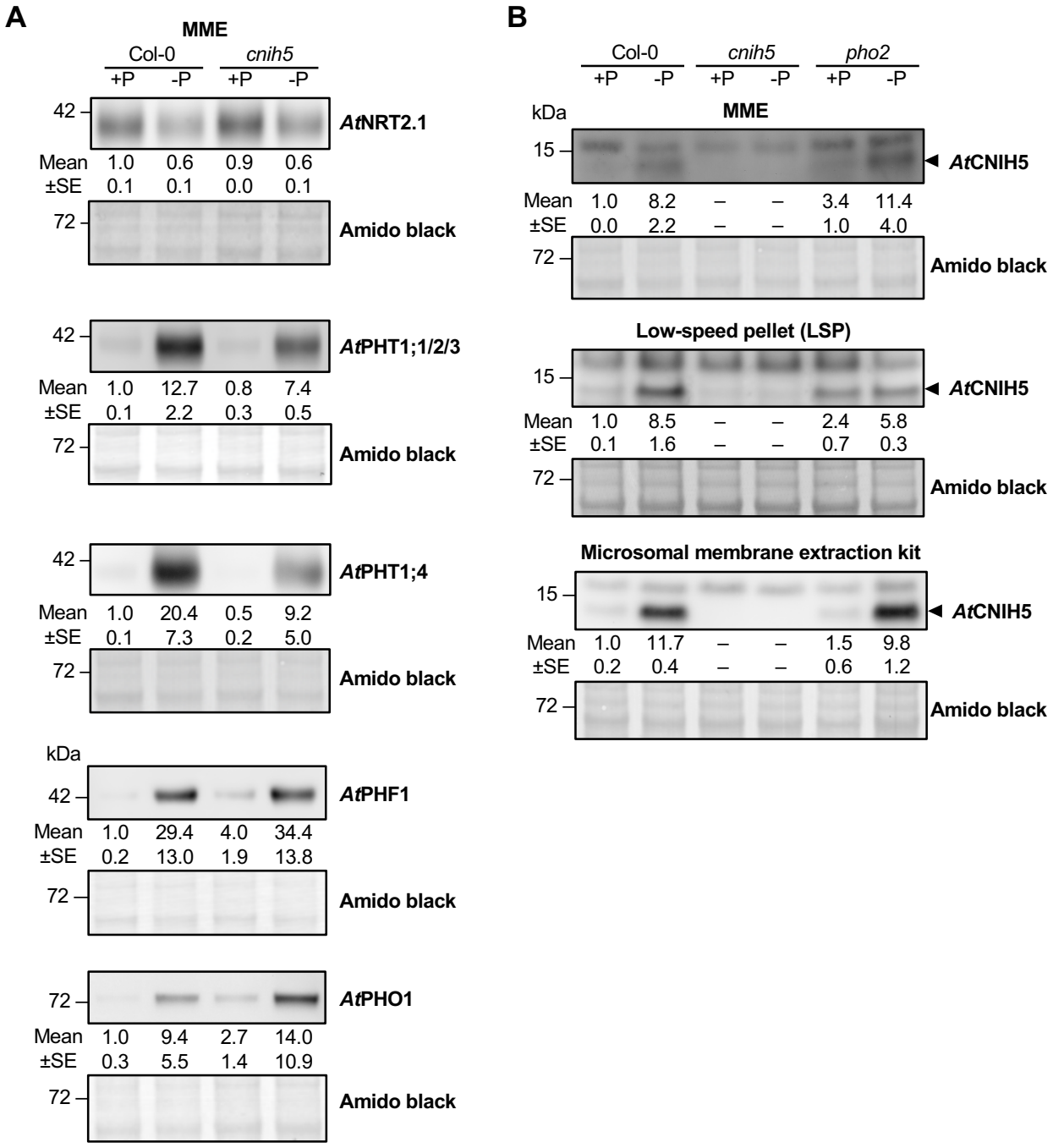

Fig 2. Immunoblot analysis of root microsomal proteins extracted from WT, *cnih5*, and *pho2* mutants. (A, B) Protein expression of *At*NRT2.1, *At*PHT1;1/2/3, *At*PHT1;4, *At*PHF1, and *At*PHO1 (A) and *At*CNIH5 (B) in the root of 11-day-old seedlings of *Arabidopsis* WT, *cnih5*, and *pho2* under +P (250 μM KH_2PO_4) and –P (0 μM KH_2PO_4, five days of starvation) conditions. The band of *At*CNIH5 is indicated by arrowhead. The relative protein expression level was normalized with the corresponding amido black staining and relative to the WT control. Error bars represent SE (n = 2–3). The applied extraction methods were shown as indicated. MME, microsomal protein extraction.

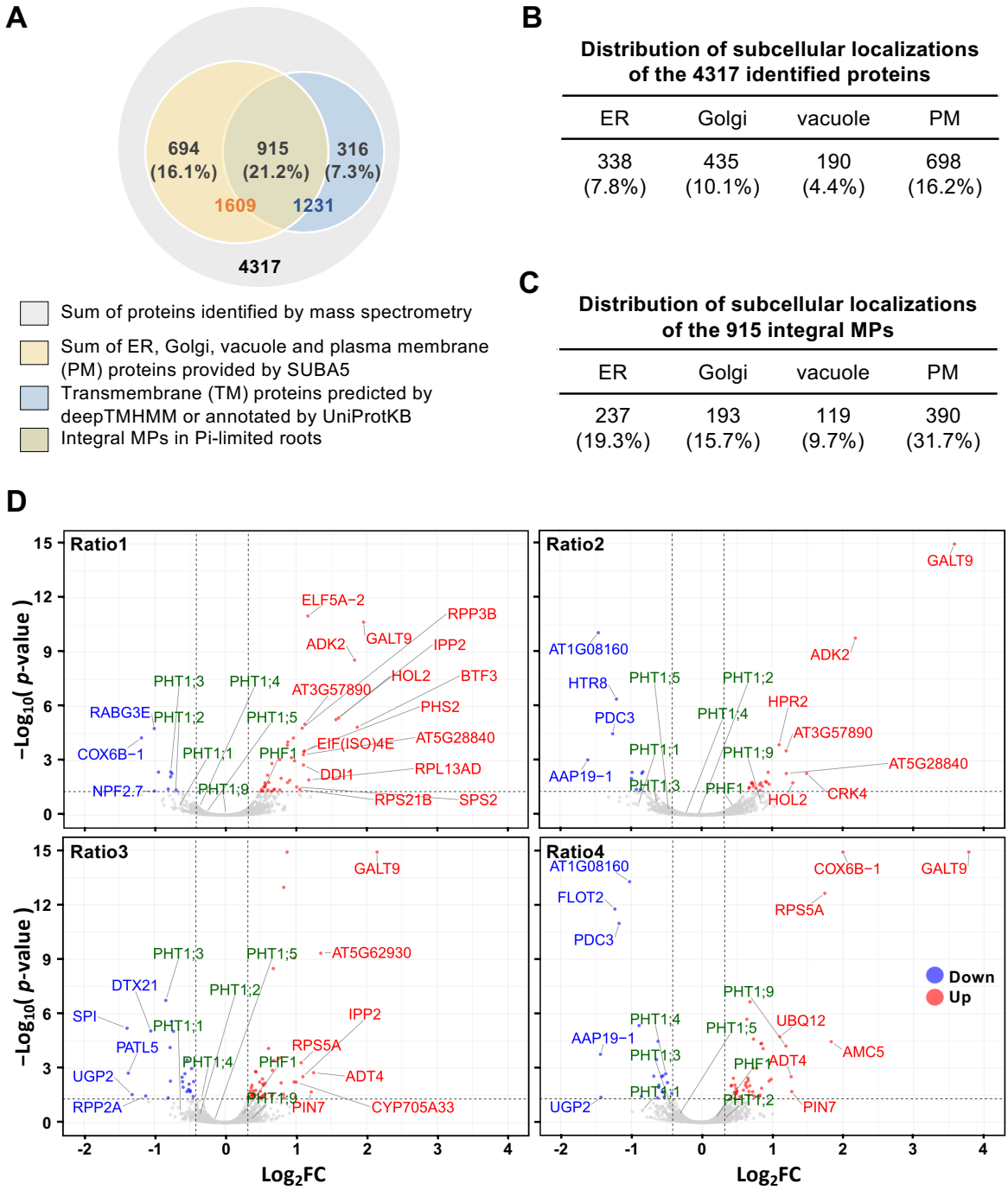

Fig 3. Summary of iTRAQ-based proteomic analysis of microsomal proteins (MPs) in Pi-limited WT and *cnih5* roots. (A) Venn diagram for comparing MPs and transmembrane (TM) proteins of the 4,317 identified proteins. Subcellular localization was analyzed by SUBA5. TM protein prediction or annotation was performed by deepTMHMM or UniprotKB. (B) Distribution of subcellular localizations of the identified 4,317 proteins analyzed by SUBA5. Note that not all proteins are restricted to a single subcellular location. (C) Distribution of subcellular localizations of the 915 integral MPs among the identified 1,231 TM proteins analyzed by SUBA5. Note that not all proteins are restricted to a single subcellular location. (D) Volcano plots of differentially expressed proteins (DEPs) in the Pi-limited root of *cnih5*. Results of the four comparison groups (four ratios of *cnih5* versus WT) were shown separately, with the $-\log_{10}$FDR adj. *p*-value plotted against the $\log_2$ fold-change (FC). The vertical dash lines denote ±1.25-FC (Log_2 FC ≈ 0.322 and Log_2FC ≈ −0.415), while the horizontal dash line denotes FDR adj. *p*-value = 0.05. Upregulated and downregulated proteins are, respectively, indicated by red and blue dots. Only DEPs with ±2-FC are marked in red or blue. The *At*PHT1s and *At*PHF1 are marked in green.

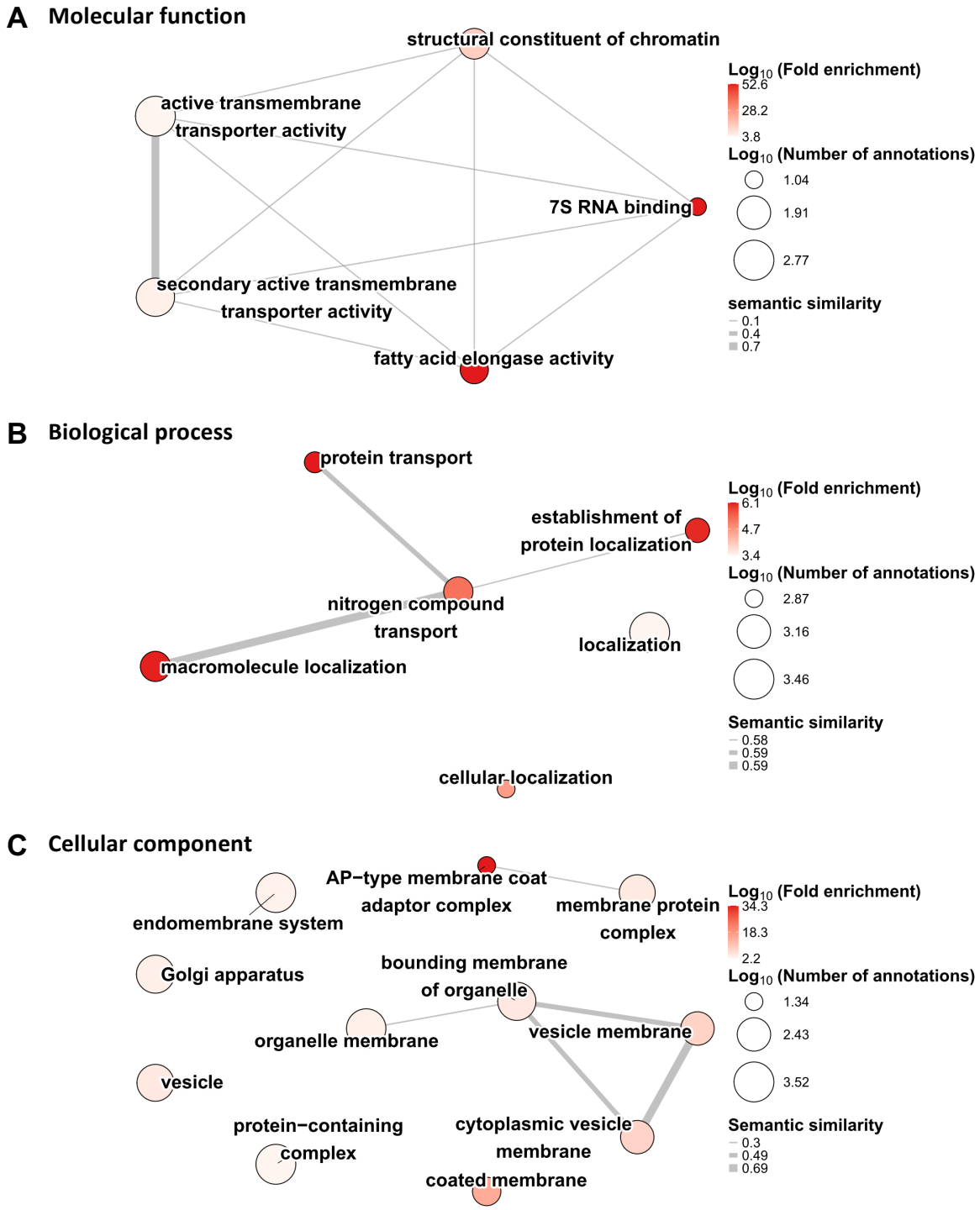

Fig 4. Interactive graph of enriched GO terms and semantic similarities for the 106 downregulated proteins in the Pi-limited *cnih5* roots. Enriched GO terms of (A) molecular function, (B) biological process, and (C) cellular component identified by ShinyGO were summarized using REVIGO to remove redundancy and cluster functionally related terms in *A. thaliana*. Each node represents a GO term, with color intensity reflecting Log_{10} (enrichment factor). The node size is proportional to the Log_{10} value of the number of gene annotations for each term in the background database. Lines between nodes represent semantic similarity, and line thickness indicates the degree of functional overlap between terms.

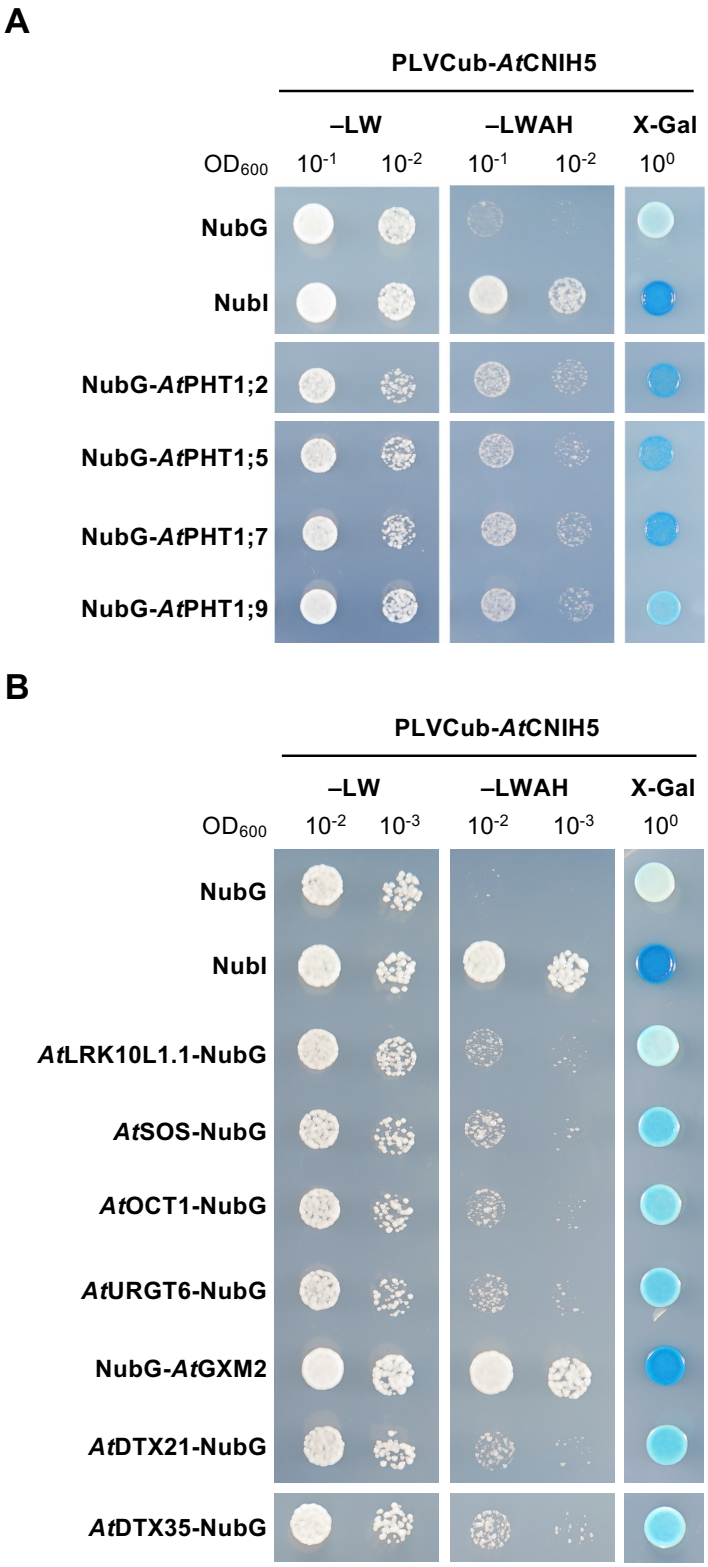

Fig 5. Analysis of the interaction of *At*CNIH5 with its potential ER cargoes by the yeast split-ubiquitin system. (A, B) Co-expression of PLVCub-*At*CNIH5 with NubG-*At*PHT1;2, NubG-*At*PHT1;5, NubG-*At*PHT1;7, and NubG-*At*PHT1;9 (A) or *At*LRK10L-1.1-NubG, *At*SOS-NubG, *At*OCT1-NubG, *At*URGT6-NubG, NubG-*At*GXM2, *At*DTX21-NubG, and *At*DTX35- NubG (B). The co-expression of PLVCub-*At*CNIH5 with NubI and NubG are used as positive and negative controls, respectively. Yeast transformants were grown on synthetic medium without leucine and tryptophan (–LW; the left panel) or on synthetic medium lacking leucine, tryptophan, adenine, and histidine with 500 μM methionine (–LWAH; middle panel) or on SC–LW containing 100 mg/L X-Gal (X-Gal; the right panel).

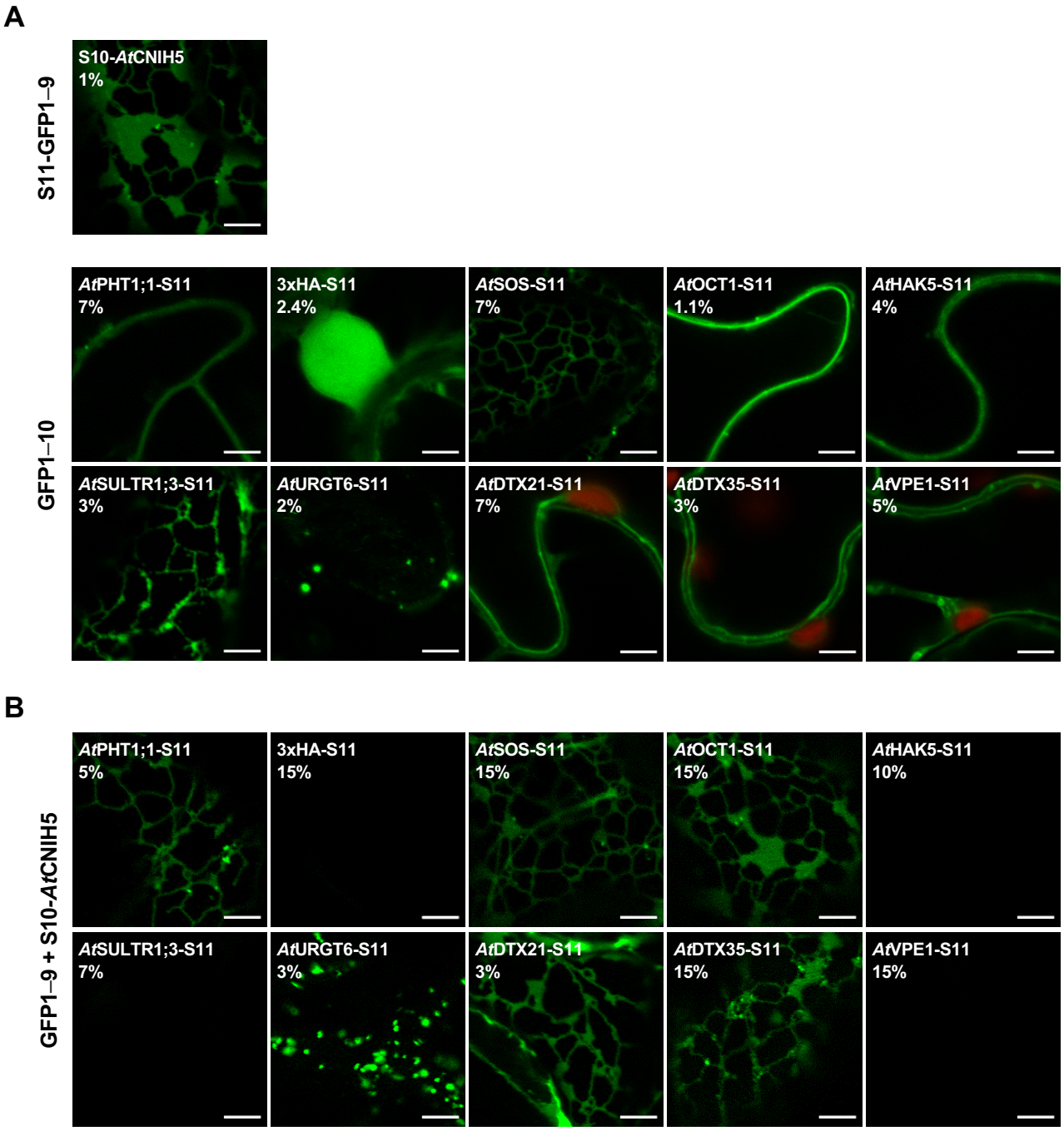

Fig 6. Analysis of the interaction of *At*CNIH5 with its potential ER cargoes by the tripartite split-GFP assay in *N. benthamiana* leaves. (A, B) Expression and subcellular localization (A) and protein–protein interaction analysis (B) of S10-*At*CNIH5 with *At*PHT1;1-S11, 3xHA-S11, *At*SOS-S11, *At*OCT1-S11, *At*HAK5-S11, *At*SULTR1;3-S11, *At*URGT6-S11, *At*DTX21-S11, *At*DTX35-S11, or *At*VPE1-S11. The co-expression of S10-*At*CNIH5 with *At*PHT1;1-S11 and 3xHA-S11 are used as positive and negative controls, respectively. The percentage of laser power used for acquisition is shown. Scale bars, 5 μm. Red signals show autofluorescence from chloroplasts.

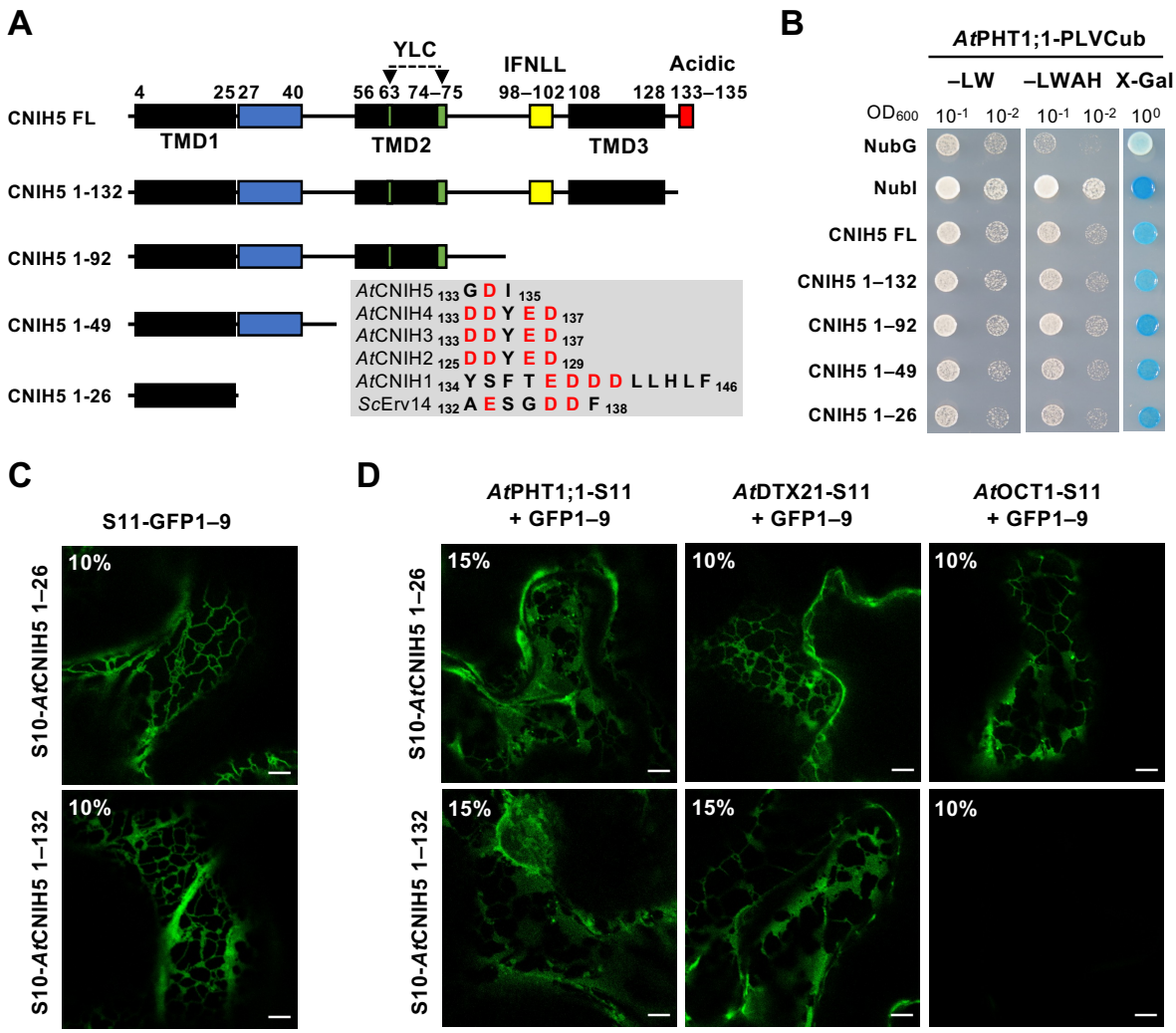

Fig 7. Analysis of the interaction of *At*PHT1;1 with the truncated *At*CNIH5 variants. (A) Schematic diagram of full-length (FL) and truncated *At*CNIH5 variants. The lengths of the truncated variants are indicated by the number of residues. The transmembrane domains and the putative cornichon, YLC, IFNLL, and acidic motifs are shown. The black box, the transmembrane domain (TMD); the blue box, the cornichon motif; the green box, the YLC motif; the yellow box, the IFNLL motif. The red box, the acidic motif. The gray box shows the sequence alignment of the putative acidic motif of *Sc*Erv14 and *At*CNIHs. Noted that *At*CNIH5 has a shorter C-terminal tail carrying only one acidic residue D134. (B) Co-expression of *At*PHT1;1-PLVCub with NubG-*At*CNIH5, NubG-*At*CNIH5 1–26, NubG-*At*CNIH5 1–49, NubG-*At*CNIH5 1–92, and NubG-*At*CNIH5 1–132 in yeast split ubiquitin assay. The co-expression of *At*PHT1;1-PLVCub with NubI and NubG are used as positive and negative controls, respectively. Yeast transformants were grown on synthetic medium without leucine and tryptophan (–LW; the left panel) or on synthetic medium lacking leucine, tryptophan, adenine, and histidine with 500 μM methionine (–LWAH; middle panel) or on SC–LW containing 100 mg/L X-Gal (X-Gal; the right panel). (C) Expression and subcellular localization of S10-*At*CNIH5 1–26 and S10-*At*CNIH5 1–132 in *N. benthamiana* leaves. (D) Protein–protein interaction analysis of *At*PHT1;1-S11, *At*DTX21-S11, or *At*OCT1-S11 with S10-*At*CNIH5 1–26 or S10-*At*CNIH5 1–132 in *N. benthamiana* leaves. The percentage of laser power used for acquisition is shown. Scale bars, 5 μm.

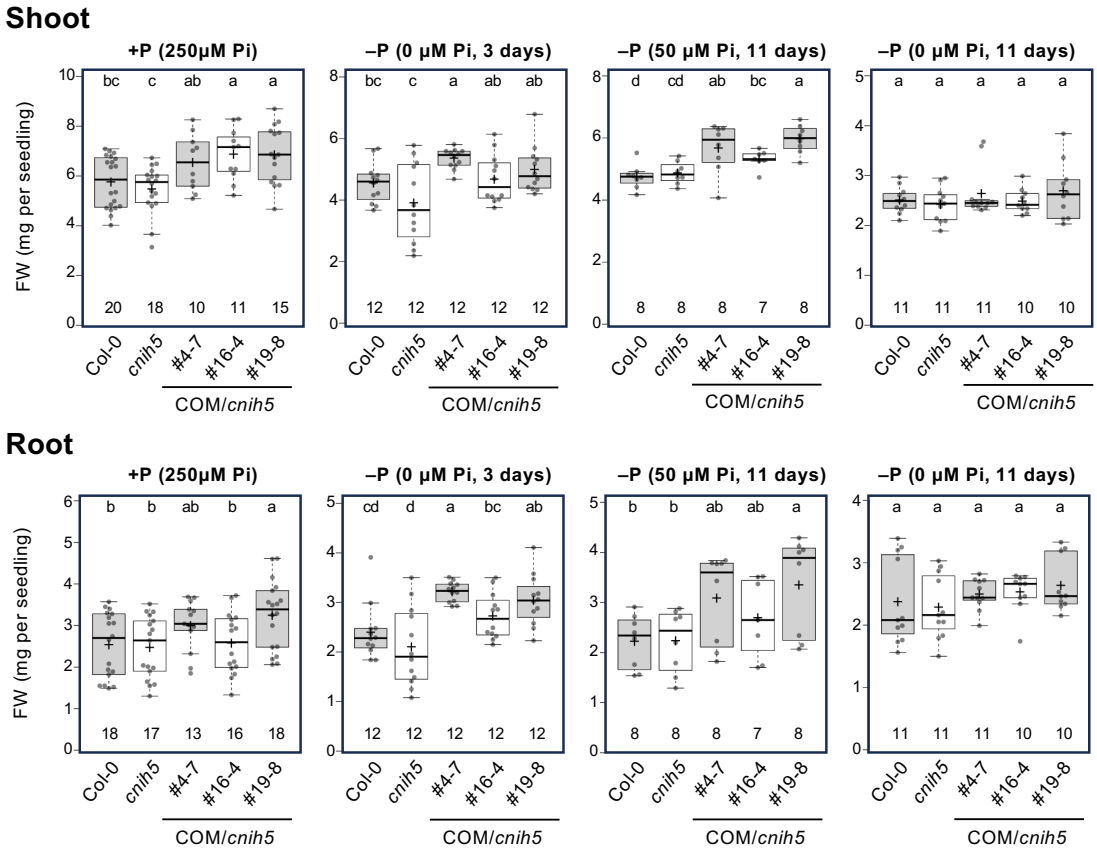

Fig 8. Increasing *in-situ At*CNIH5 expression/activity boosts plant growth.
The shoot and root fresh weight (FW) of *Arabidopsis* 11-day-old WT, *cnih5* and *AtCNIH5pro*: GFP-*AtCNIH5/cnih5* complementation (COM) lines under +P (250 µM KH_2PO_4), modest –P (0 µM KH_2PO_4, three days of starvation or 50 µM KH_2PO_4, eleven days of starvation), and severe –P (0 µM KH_2PO_4, eleven days of starvation) conditions. Data are visualized using BoxPlotR (Spitzer *et al.*, 2014). Center lines show the medians; the central plus signs (+) show the means; box limits indicate the 25th and 75th percentiles; whiskers extend to the 5th and 95th percentiles, and data points are plotted as dots. Data significantly different from the other groups are indicated by different lowercase letters (n, pools of seedings from independent experiments; One-Way ANOVA, Duncan's test).

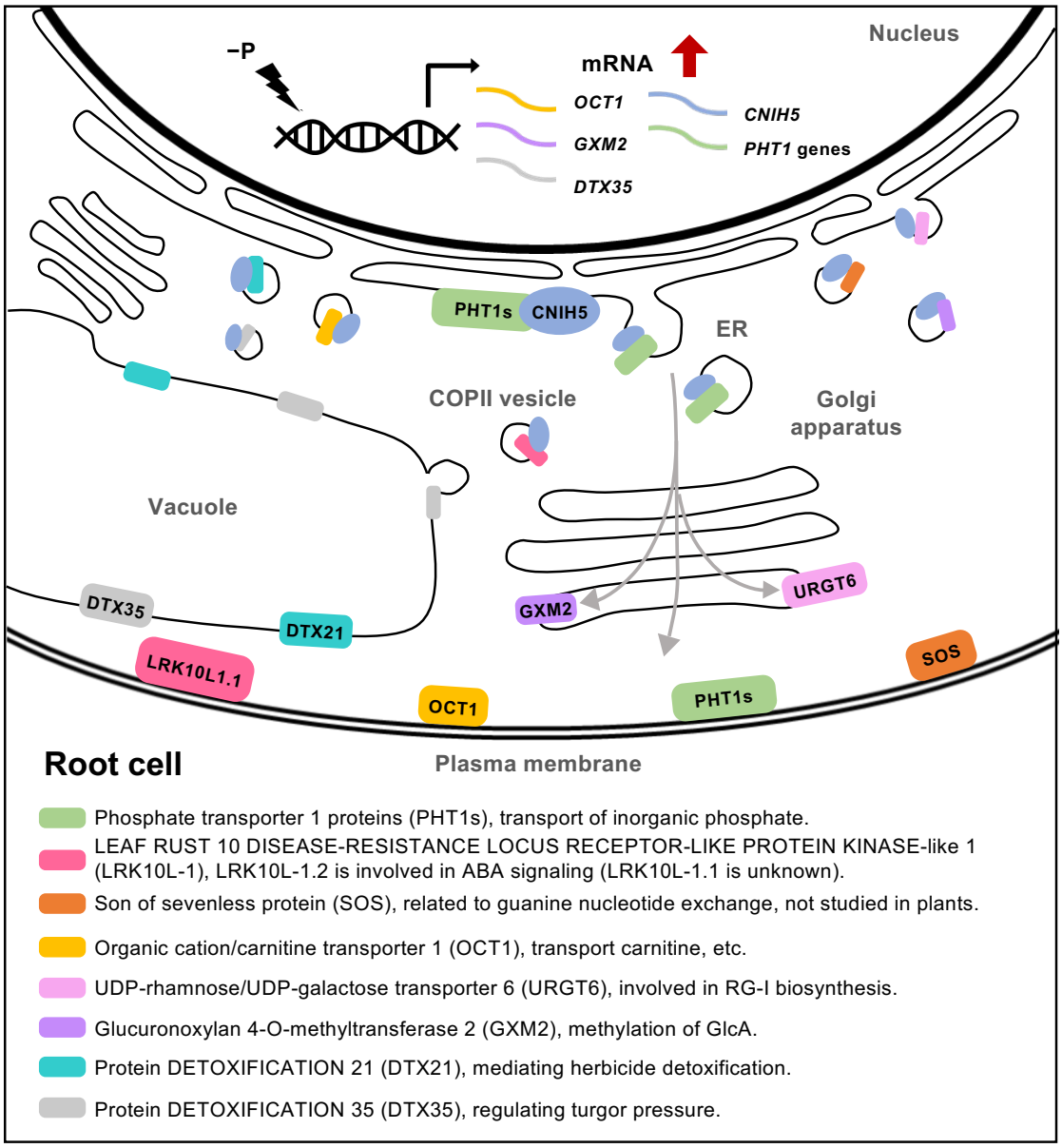

Fig. 9. *At*CNIH5-mediated ER-to-Golgi transport of membrane proteins associated with Pi starvation responses in *Arabidopsis* root.

Under Pi starvation (−P), the transcripts of *CNIH5*, *PHT1* genes, *OCT1*, *GXM2*, and *DTX35* increase in *Arabidopsis* root cells . As an ER cargo receptor, CNIH5 assists the ER export of the newly synthesized PHT1s, LRK10L-1.1, SOS, OCT1, URGT6, GXM2, DTX21, and DTX35, and their loading into COPII vesicles, thereby directing them to their corresponding subcellular destinations.

Table 1. Summary of *At*PHT1s and *At*PHF1 abundance in Pi-limited WT and *cnih5* roots.
The normalized ratios compared the protein expression in Col-0_1, Col-0_2, *cnih5*_1 and *cnih5*_2 samples. The FDR adj. *p*-values are in parentheses.

Accession	Gene name	AGI code	Coverage [%]	Unique peptides	*cnih5*_1 /Col-0_1	*cnih5*_2 /Col-0_1	*cnih5*_1 /Col-0_2	*cnih5*_2 /Col-0_2
Q8VYM2	*AtPHT1;1*	AT5G43350	38	2	0.63 (0.41)	0.54 (0.28)	0.65 (0.31)	0.56 (0.22)
Q96243	*AtPHT1;2*	AT5G43370	30	1	0.61 (0.05)	0.97 (1.00)	0.78 (0.47)	1.24 (0.67)
O48639	*AtPHT1;3*	AT5G43360	10	2	0.58 (0.00)	0.65 (0.24)	0.56 (0.00)	0.74 (0.14)
Q96303	*AtPHT1;4*	AT2G38940	12	6	0.77 (0.40)	0.86 (0.89)	0.79 (0.06)	0.70 (0.00)
Q8GYF4	*AtPHT1;5*	AT2G32830	6	2	0.82 (0.78)	0.73 (0.58)	0.90 (0.87)	0.80 (0.42)
Q9S735	*AtPHT1;9*	AT1G76430	5	2	1.00 (0.99)	1.79 (0.20)	1.27 (0.79)	2.88 (0.00)
Q8GYE0	*AtPHF1*	AT3G52190	40	13	1.45 (0.05)	1.37 (0.36)	1.16 (0.48)	1.14 (0.62)

Coverage [%]: The percentage of the protein sequences covered by identified peptides.

Unique peptides: The total number of distinct peptide sequences unique to the protein group.

Table 2. List of the 31 downregulated microsomal transmembrane proteins in Pi-limited *cnih5* roots.
The normalized ratios compared the protein expression in Col-0_1, Col-0_2, *cnih5*_1 and *cnih5*_2 samples. The FDR adj. *p*-values are in parentheses. The candidates highlighted in gray are selected for testing protein–protein interaction in this study. Subcellular localization is predicted or annotated by SUBA5, UniprotKB or experimental data.

AGI code	Accession	Gene name	*cnih5*_1/ Col-0_1	*cnih5*_2/ Col-0_1	*cnih5*_1/ Col-0_2	*cnih5*_2/ Col-0_2
		ER				
AT1G04220	Q5XEP9	3-ketoacyl-CoA synthase 2 (*AtKCS2*)	0.73 (0.57)	0.72 (0.66)	0.99 (0.99)	0.98 (1.00)
AT1G34130	Q9FX21	Dolichyl-diphosphooligosaccharide--protein glycosyltransferase subunit STT3B (*AtSTT3B*)	0.75 (0.53)	0.65 (0.30)	0.91 (0.91)	0.77 (0.38)
AT1G51740	P59277	Syntaxin-81 (*AtSYP81*)	1.18 (0.97)	0.73 (0.88)	0.94 (0.98)	0.58 (0.52)
AT3G23175	Q8GYI3	HR-like lesion-inducing protein-like protein	0.68 (0.23)	0.69 (0.46)	0.94 (0.97)	0.96 (0.99)
AT3G23190	Q9LTC9	HR-like lesion-inducing protein-like protein	0.94 (0.99)	0.63 (0.20)	0.92 (0.92)	0.62 (0.00)
AT3G48570	Q9SMP2	Protein transport protein Sec61 subunit gamma-3 (*AtSEC61G3*)	0.72 (0.30)	0.69 (0.42)	0.71 (0.02)	0.72 (0.12)
AT4G14420	O23298	HR-like lesion-inducing protein-like protein	0.76 (0.53)	0.61 (0.07)	0.81 (0.30)	0.64 (0.00)
AT5G43760	Q9FG87	3-ketoacyl-CoA synthase 20 (*AtKCS20*)	1.03 (1.00)	0.60 (0.54)	1.23 (0.93)	0.72 (0.80)
		Golgi				
AT1G34020	Q9FDZ5	UDP-rhamnose/UDP-galactose transporter 6 (*AtURGT6*)	0.60 (0.49)	0.45 (0.18)	0.68 (0.69)	0.50 (0.27)
AT2G03480	Q3EC77	QUASIMODO2 LIKE 2 (*AtQUL2*)	0.78 (0.73)	0.64 (0.35)	0.87 (0.86)	0.68 (0.27)
AT2G40380	Q9SIY7	Prenylated Rab acceptor 1 (PRA1) family protein B2 (*AtPRA1B2*)	0.66 (0.26)	0.74 (0.72)	0.94 (0.97)	1.05 (0.99)
AT4G09990	Q9T0F7	Glucuronoxylan 4-O-methyltransferase 2 (*AtGXM2*)	0.71 (0.76)	0.73 (0.87)	0.58 (0.36)	0.60 (0.54)
AT4G30440	Q9M0B6	UDP-glucuronate 4-epimerase 1 (*AtGAE1*)	0.83 (0.93)	0.64 (0.58)	0.88 (0.93)	0.68 (0.38)
AT4G38270	Q0WQD2	Galacturonosyltransferase 3 (*AtGAUT3*)	0.87 (0.92)	0.62 (0.32)	0.95 (0.98)	0.69 (0.17)
AT5G25100	Q9C5N2	Transmembrane 9 superfamily member 9 (*AtTMN9*)	0.73 (0.69)	0.81 (0.89)	0.70 (0.33)	0.78 (0.62)
		Vacuole				
AT1G33110	Q8W488	Protein DETOXIFICATION 21 (*AtDTX21*)	0.52 (0.00)	0.76 (0.77)	0.48 (0.00)	0.71 (0.40)
AT4G17340	Q41975	Tonoplast intrinsic protein 2;2 (*AtTIP2-2*)	0.88 (0.95)	0.91 (0.97)	0.65 (0.34)	0.64 (0.40)
AT4G25640	F4JTB3	Protein DETOXIFICATION 35 (*AtDTX35*)	0.86 (0.89)	0.66 (0.31)	0.89 (0.83)	0.68 (0.02)
AT5G46090	Q9FNL3	DUF679 domain membrane protein 6 (*AtDMP6*)	0.74 (0.39)	0.64 (0.22)	0.86 (0.65)	0.74 (0.17)
		PM				
AT1G05570	Q9AUE0	Callose synthase 1 (*AtCALS1*)	0.74 (0.60)	0.73 (0.66)	0.82 (0.72)	0.80 (0.75)
AT1G17620	Q9LNP3	Late embryogenesis abundant (LEA) hydroxyproline-rich glycoprotein family	0.73 (0.54)	0.61 (0.23)	0.93 (0.96)	0.78 (0.68)
AT1G18390	P0C5E2	LEAF RUST 10 DISEASE-RESISTANCE LOCUS RECEPTOR-LIKE PROTEIN KINASE-like 1.2 (*AtLRK10L-1.2*)	0.74 (0.35)	0.72 (0.53)	0.75 (0.09)	0.73 (0.15)
AT1G26650	Q9LQY7	Son of sevenless protein (*AtSOS*)	0.61 (0.22)	0.70 (0.70)	0.61 (0.09)	0.70 (0.27)
AT1G73220	Q9CAT6	Organic cation/carnitine transporter 1 (*AtOCT1*)	0.89 (0.93)	0.86 (0.93)	0.73 (0.04)	0.69 (0.05)
AT2G27140	Q9ZVC6	HSP20-like chaperones superfamily protein	1.00 (0.99)	0.61 (0.13)	1.11 (0.87)	0.65 (0.01)
AT3G02600	Q8LFD1	Lipid phosphate phosphatase 3 (*AtLPP3*)	0.89 (0.92)	0.62 (0.16)	0.97 (0.98)	0.68 (0.02)
AT3G61270	Q9M2D7	Glycosyltransferase (*AtT20K12.170*)	0.84 (0.89)	0.67 (0.46)	0.80 (0.58)	0.64 (0.13)
AT4G01830	Q9SYI3	ATP binding cassette (ABC) transporter B family member 5 (*AtABCB5*)	0.75 (0.79)	0.68 (0.71)	0.99 (1.00)	1.03 (1.00)
AT5G20970	F4K6X6	HSP20-like chaperones superfamily protein	0.85 (0.86)	0.51 (0.00)	1.10 (0.89)	0.66 (0.01)
AT5G43350	Q8VYM2	Inorganic phosphate transporter 1;1 (*AtPHT1;1*)	0.63 (0.41)	0.54 (0.28)	0.65 (0.31)	0.56 (0.22)
AT5G43360	O48639	Inorganic phosphate transporter 1;3 (*AtPHT1;3*)	0.58 (0.00)	0.65 (0.24)	0.56 (0.00)	0.74 (0.14)